PHYSICAL REVIEW RESEARCH **7**, 033214 (2025)

Optical non-Hermitian skin effect in uniform media

Taiki Yoda,[1] Yuto Moritake,[1] Kenta Takata,[2,3] Kazuki Yokomizo,[4] Shuichi Murakami,[1] and Masaya Notomi[1,2,3,*]
[1]*Department of Physics, Tokyo Institute of Technology, 2-12-1 Ookayama, Meguro-ku, Tokyo 152-8551, Japan*
[2]*NTT Basic Research Laboratories, NTT Corporation, 3-1 Morinosato-Wakamiya, Atsugi, Kanagawa 243-0198, Japan*
[3]*Nanophotonics Center, NTT Corporation, 3-1 Morinosato-Wakamiya, Atsugi, Kanagawa 243-0198, Japan*
[4]*Department of Physics, The University of Tokyo, 7-3-1 Hongo, Bunkyo-ku, Tokyo 113-0033, Japan*

(Received 17 March 2023; accepted 5 August 2025; published 3 September 2025)

Non-Hermitian skin effect (NHSE), which is a localization phenomenon in non-Hermitian systems, has recently been of great interest. Most previous works in various systems studied periodic systems. However, electromagnetic waves do not feel the periodicity of a system if the wavelength is sufficiently long, and it has not been clear that electromagnetic waves exhibit the localization caused by the non-Hermiticity itself even in uniform systems without the periodicity. Here, we establish the theory of the optical NHSE in non-Hermitian uniform media and show that the optical NHSE occurs even in uniform media. We apply our theory to subwavelength metamaterials and demonstrate the existence of a non-Hermitian skin mode in a multilayer metamaterial. Finally, we propose a concept of a stationarily excited skin mode to describe a lossy system under stationary excitation with real excitation frequency.

DOI: 10.1103/3tlp-16mc

I. INTRODUCTION

Non-Hermitian systems with gain and/or loss have been extensively investigated because non-Hermiticity often leads to phenomena without counterparts in Hermitian systems [1–4]. Recent studies have shown that "bulk" eigenstates are localized at the boundary of systems in certain non-Hermitian periodic systems and that their localized states form continuous spectra in spite of the localization. Such peculiar localized phenomenon is called the non-Hermitian skin effect (NHSE) [5–17]. The NHSEs have been demonstrated experimentally in various systems, including mechanics [18–20], electric circuits [21–24], quantum walk [25,26], acoustics or phononics [27–30], and photonics [31]. Most previous works related to the NHSE have discussed periodic systems because the NHSE stems from condensed matter physics. However, in contrast to electrons in solids, electromagnetic waves often propagate in an optically uniform medium with a position-independent dielectric permittivity such as bulk materials and metamaterials. Therefore, in the field of optics (and other classical wave systems), it is significant whether electromagnetic waves are localized by the non-Hermiticity itself even in uniform systems without periodic modulation.

In this paper, we establish the theory of optical NHSE in uniform media and show that the optical NHSE occurs even in a uniform anisotropic medium with gain and/or loss. The combination of the anisotropy and non-Hermiticity of a dielectric tensor acts as an effective imaginary gauge potential for electromagnetic waves, and it induces the localization of electromagnetic waves caused by the non-Hermiticity itself. Our theory offers the simplest physical system where the NHSE occurs among ever reported. By realizing the NHSE in this simple system, we can clarify the essence of the NHSE and derive phenomena from the model. First, our theory can be applied to subwavelength metamaterials described by the effective medium theory. We particularly propose multilayer metamaterials as a platform for realizing the optical NHSE. Second, we extend our analytical formulation of the NHSE of eigenstates with complex frequencies to stationarily excited states with real frequencies. Previous works related to the NHSE in two-dimensional systems [6,11,13–16,32–39] investigated the localization of eigenstates with generally complex eigenvalues. However, these theories cannot be applied to lossy systems under stationary excitation such as transmission and reflection measurements because the frequency of excited electromagnetic waves is forced to be real under stationary excitation even in lossy systems. To overcome this mismatch, we propose a concept of a stationarily excited skin mode with a real frequency and a complex wave vector, and find that the NHSE occurs even under this condition. Surprisingly, the localization length of a non-Hermitian skin mode depends on whether the wave vector in a propagation direction is real or complex.

II. THEORY OF NON-HERMITIAN SKIN EFFECT IN BOUNDED UNIFORM MEDIA

A. Analytical solution with spatial boundary

The propagation of electromagnetic waves in a uniform medium is governed by a dielectric tensor. The energy of electromagnetic waves is generally not conserved in a system with a non-Hermitian dielectric tensor [40]. In this paper,

---

[*] Contact author: notomi@phys.sci.isct.ac.jp

we focus on uniform media with a non-Hermitian dielectric tensor given by

$$\begin{pmatrix} \varepsilon_{xx} & \varepsilon_{xy} & 0 \\ \varepsilon_{yx} & \varepsilon_{yy} & 0 \\ 0 & 0 & \varepsilon_{zz} \end{pmatrix}, \tag{1}$$

where x, y, and z represent the spatial coordinates. The magnetic permeability is assumed to be unity. We denote the upper-left block of Eq. (1) as ε. The dielectric tensor (1) is Hermitian when ε satisfies $\varepsilon_{xx} = \varepsilon_{xx}^*$, $\varepsilon_{yy} = \varepsilon_{yy}^*$, and $\varepsilon_{xy} = \varepsilon_{yx}^*$. We neglect ε_{zz} because it does not affect transverse electric (TE) modes. The dielectric tensor could be reciprocal or nonreciprocal, and we will discuss the effect of reciprocity later. In this paper, we consider two-dimensional systems where electromagnetic waves are invariant in the z direction. When electromagnetic waves propagate within the xy plane in the media, TE modes and transverse magnetic modes are decoupled from each other. The uniform solution of TE modes in the y direction, which is expressed as $H_z(x, y, t) = \exp[i(\omega t - k_y y)]H_z(x)$, satisfies the following equation [13]:

$$\hat{\Theta}(k_y)H_z(x) = \left(\frac{\omega}{c}\right)^2 H_z(x), \tag{2}$$

$$\hat{\Theta}(k_y) = -\eta_{yy}\frac{d^2}{dx^2} - ik_y(\eta_{xy} + \eta_{yx})\frac{d}{dx} + \eta_{xx}k_y^2, \tag{3}$$

$$\begin{pmatrix} \eta_{xx} & \eta_{xy} \\ \eta_{yx} & \eta_{yy} \end{pmatrix} = \frac{1}{\varepsilon_{xx}\varepsilon_{yy} - \varepsilon_{xy}\varepsilon_{yx}}\begin{pmatrix} \varepsilon_{yy} & -\varepsilon_{xy} \\ -\varepsilon_{yx} & \varepsilon_{xx} \end{pmatrix}, \tag{4}$$

where ω is the angular frequency, t represents the time, k_y is the y component of the wave vector, c is the speed of light in vacuum, and η is the inverse tensor of ε. From the viewpoint of electromagnetics, the non-Hermiticity of ε leads to material gain and/or loss. On the other hand, the non-Hermiticity of $\hat{\Theta}$ leads to the imaginary part of the eigenfrequency ω. Therefore, the non-Hermiticity of $\hat{\Theta}$ is determined by the non-Hermiticity of ε. Here, k_y is assumed to be real by analogy with the Bloch wave vector in periodic systems. Equations (2) and (3) take the similar form to the one-dimensional time-independent Schrödinger equation with a gauge potential because Eq. (2) is a second-order differential equation with a first derivative term. The first term in Eq. (3) corresponds to a kinetic-energy term, and the third term corresponds to a constant potential-energy term. The second term corresponds to an effective gauge potential for photon induced by the anisotropy of a dielectric tensor [13,41,42]. Therefore, electromagnetic waves in anisotropic media can potentially emulate the dynamics of free electrons in a uniform gauge potential. The non-Hermiticity of ε is a necessary condition for the non-Hermiticity of $\hat{\Theta}(k_y)$. The first derivative in Eq. (3) gives spatial asymmetry of a system along the x direction and can be effectively regarded as asymmetric hopping in tight-binding models [5,7–10]. A tight-binding model is reduced to a continuous model in the limit where the lattice constant is zero, and in this limit an asymmetric hopping corresponds to a first derivative in this limit.

The anti-Hermitian part of an effective gauge potential causes peculiar localization of eigenmodes like electrons in an imaginary gauge potential [43]. To see this, we consider uniform systems that are finite in the x direction with a size L and infinite in the y direction. As was clarified previously, the eigenfrequency and mode profile are sensitive to boundary conditions in non-Hermitian systems. Eigenmodes are always extended for the periodic boundary condition (PBC) having an infinite medium size, but localized skin modes generally appear for finite-sized boundary conditions. We first impose the periodic boundary condition $H_z(0) = H_z(L)$. The PBC quantizes the wave vector k_x to $2\pi n/L$, and we obtain

$$k_x = \frac{2\pi n}{L}, \quad n = 0, \pm 1, \pm 2, \ldots, \tag{5}$$

$$\left(\frac{\omega_{\mathrm{PBC}}}{c}\right)^2 = \eta_{yy}(k_x + qk_y)^2 + (\eta_{xx} - q^2\eta_{yy})k_y^2, \tag{6}$$

$$q = -\frac{\eta_{xy} + \eta_{yx}}{2\eta_{yy}} = \frac{\varepsilon_{xy} + \varepsilon_{yx}}{2\varepsilon_{xx}}, \tag{7}$$

where we explicitly define the dimensionless parameter q. Equation (6) is the dispersion relation of a plane-wave solution with a real k_x. It follows from Eq. (6) that qk_y corresponds to the effective gauge potential because it shifts the wave vector k_x. The parameter q is an important quantity in our work, which essentially determines the strength of the effective gauge potential for each medium. By definition, the effective gauge potential can be drastically enhanced when $|\varepsilon_{xx}| \approx 0$.

Under the PBC, the wave vector k_x becomes real and thus the electromagnetic wave is extended over the system. However, the delocalization of the eigenmode does not necessarily hold under other boundary conditions. The general solution of Eq. (2) is expressed by the superposition of two plane waves:

$$H_z(x) = Ae^{-ik_+x} + Be^{-ik_-x}, \tag{8}$$

$$E_x(x) = -(Z_{y+}Ae^{-ik_+x} + Z_{y-}Be^{-ik_-x}), \tag{9}$$

$$E_y(x) = Z_{x+}Ae^{-ik_+x} + Z_{x-}Be^{-ik_-x}. \tag{10}$$

Here, $k_\pm$, $Z_{x\pm}$, and $Z_{y\pm}$ are defined by

$$Z_{y\pm} = \frac{1}{\omega\varepsilon_0}(k_y\eta_{xx} - k_\pm\eta_{xy}), \tag{11}$$

$$Z_{x\pm} = \frac{1}{\omega\varepsilon_0}(-k_y\eta_{yx} + k_\pm\eta_{yy}), \tag{12}$$

$$k_\pm = -qk_y \pm \alpha, \tag{13}$$

$$\alpha = \sqrt{\frac{1}{\eta_{yy}}\left\{\left(\frac{\omega}{c}\right)^2 - (\eta_{xx} - q^2\eta_{yy})k_y^2\right\}}, \tag{14}$$

where ε_0 is the permittivity of vacuum. k_+ (k_-) is the solution of Eq. (2) for given ω and k_y, and it represents the wave vector of a plane wave propagating in the $+x$ ($-x$) direction. The two wave vectors satisfy $k_- \neq -k_+$ when $q \neq 0$ [44–47]. The value of $k_\pm$ is determined by boundary conditions. As a specific example, let us consider a system sandwiched by two perfect electric conductors (PECs) placed at $x = 0$ and L. The two PECs require $E_y(0) = E_y(L) = 0$, which quantizes the difference of the wave vectors as $k_+ - k_- = 2\alpha = 2\pi n/L$. By combining $k_+ + k_- = -2qk_y$, we obtain

$$k_\pm = \pm\frac{\pi n}{L} - qk_y, \quad n = 1, 2, \ldots. \tag{15}$$

TABLE I. Comparison of PBC and PEC.

	k_x	$(\omega/c)^2$	$E_y(x)$
PBC	$\frac{2\pi n}{L}$	$\eta_{yy}(k_x+qk_y)^2+$ $(\eta_{xx}-q^2\eta_{yy})k_y^2$	$e^{-ik_x x}$
PEC	$\pm\frac{\pi n}{L}-qk_y$	$\eta_{yy}(\pi n/L)^2+$ $(\eta_{xx}-q^2\eta_{yy})k_y^2$	$e^{iqk_y x}\sin\left(\frac{\pi nx}{L}\right)$

Inserting Eq. (15) into Eqs. (8)–(10) and (14) yields

$$\left(\frac{\omega_{\mathrm{PEC}}}{c}\right)^2=\eta_{yy}\left(\frac{\pi n}{L}\right)^2+(\eta_{xx}-q^2\eta_{yy})k_y^2, \tag{16}$$

$$E_y(x)=e^{iqk_y x}\sin\left(\frac{\pi n}{L}x\right), \tag{17}$$

$$\begin{aligned}H_z(x)=\frac{1}{2}ie^{iqk_y x}\Bigg[&\left(\frac{1}{Z_{x+}}-\frac{1}{Z_{x-}}\right)\cos\left(\frac{\pi n}{L}x\right)\\&-i\left(\frac{1}{Z_{x+}}+\frac{1}{Z_{x-}}\right)\sin\left(\frac{\pi n}{L}x\right)\Bigg],\end{aligned} \tag{18}$$

$$\begin{aligned}E_x(x)=-\frac{1}{2}ie^{iqk_y x}\Bigg[&\left(\frac{Z_{y+}}{Z_{x+}}-\frac{Z_{y-}}{Z_{x-}}\right)\cos\left(\frac{\pi n}{L}x\right)\\&-i\left(\frac{Z_{y+}}{Z_{x+}}+\frac{Z_{y-}}{Z_{x-}}\right)\sin\left(\frac{\pi n}{L}x\right)\Bigg].\end{aligned} \tag{19}$$

Because the dielectric tensor [Eq. (1)] is twofold rotational symmetric around the z axis, ω_{PEC} always satisfies $\omega_{\mathrm{PEC}}(k_y)=\omega_{\mathrm{PEC}}(-k_y)$. Equations (15)–(19) are one of the main results of our work. First, Eq. (15) shows that the wave vectors $k_\pm$ are shifted from $\pm\pi n/L$ by the effective gauge potential, and that they necessarily become complex when $\mathrm{Im}(qk_y)\neq 0$. The imaginary part of $k_\pm$ is given by $\mathrm{Im}(k_+)=\mathrm{Im}(k_-)=-\mathrm{Im}(qk_y)$. Second, Eqs. (17)–(19) show that all the eigenmodes are localized at a boundary of the system when $\mathrm{Im}(qk_y)\neq 0$ because the amplitude of E_y is written as $|E_y(x)|=\exp[-\mathrm{Im}(qk_y)x]|\sin(\pi nx/L)|$. The envelope of the eigenmode decays exponentially and its localization strength is given by $|\mathrm{Im}(k_\pm)|=|\mathrm{Im}(qk_y)|$. The sign of $\mathrm{Im}(qk_y)$ determines which side the eigenmode is localized at. Third, the trajectory of complex ω_{PEC} in the complex eigenfrequency plane disagrees with ω_{PBC} even in the limit of $L\to\infty$ when $\mathrm{Im}(qk_y)\neq 0$. The trajectory of ω_{PEC}^2 is always a semi-infinite line on the complex-ω^2 plane, while the trajectory of ω_{PBC}^2 is a parabola when $\mathrm{Im}(qk_y)\neq 0$. The two trajectories coincide with each other when $\mathrm{Im}(qk_y)=0$. The detailed proof is presented in Appendix A. These results hold for a perfect magnetic conductor (PMC) condition (see Appendix B). The localization will appear for other open boundary conditions such as air cladding although the analytical expression of its localization length cannot be derived [11,15]. It is not guaranteed that the localization strength is determined by $\mathrm{Im}(qk_y)$ for the case of other boundary conditions. The comparison of PBC and PEC is summarized in Table I.

The localization phenomenon discussed above has the same features as the NHSE in periodic systems. For the NHSE in periodic systems, the localization of a skin mode is described by the non-Bloch band theory [5–7,10,12,13,39]. The non-Bloch band theory extends the Bloch wave vector to the complex number, which corresponds to Eq. (15). The imaginary part of a Bloch wave vector determines the localization strength and localized position of a skin mode. Although such explanations may seem valid only for periodic systems, essentially the same explanations are valid in our uniform systems when we replace a Bloch wave vector with wave vectors as shown in Eqs. (15) and (17)–(19). For the NHSE in periodic systems, the eigenvalue under the PBC disagrees with that under an open boundary condition, which corresponds to Eqs. (6) and (16). Recently, the topological property of NHSE in the periodic systems has gathered interest [9]. One can discuss a similar topological property of NHSE in uniform media by introducing a winding number [48]. In contrast to periodic systems, the notion of the Brillouin zone cannot be applied to uniform systems. The real part of the Bloch wave vector is bounded within the first Brillouin zone and it forms a closed loop in the momentum space, while the real part of $k_\pm$ is not bounded. For the NHSE in periodic systems, the eigenvalue under the PBC forms a finite or infinite number of closed loops in the complex eigenvalue plane, and the winding number can be defined for each closed loop [8,9]. For the NHSE in uniform media, the eigenvalue under the PBC forms an open arc in the complex eigenvalue space because the real part of $k_\pm$ itself does not form a closed loop in the momentum space. Nevertheless, we can prove that the eigenfrequency of a skin mode appears inside an open arc drawn by the trajectory of ω_{PBC}, and an open arc can be characterized by the winding number [48]

$$W(k_y,\omega_0)=\int_{-\infty}^{\infty}\frac{dk_x}{2\pi}\arg[\omega_{\mathrm{PBC}}^2(k_x,k_y)-\omega_0^2], \tag{20}$$

where ω_0^2 is a reference point on the complex-ω^2 plane. The winding number W is finite when ω_0^2 is inside an open arc, and its value is $-\mathrm{sgn}[\mathrm{Im}(qk_y)]$. The detailed proof is given in Appendix C. The direction of a parabola and the sign of the winding number are closely related to the localized position of a skin mode because they are given by the sign of $\mathrm{Im}(qk_y)$. Consequently, the localization phenomenon described by Eqs. (17)–(19) is considered as the NHSE in uniform media. We note that the topological nature of uniform media has been discussed in the context of the topological Chern number [49], where k space of uniform media is regarded as the Riemann sphere. This treatment can also be applied to our discussion to define the point gap topology in uniform media.

The skin mode in uniform media is qualitatively different from surface localized waves in uniform media such as surface plasmon polaritons (SPPs). For a given k_y, an SPP has discrete spectrum while a skin mode forms continuous spectrum in the limit of $L\to\infty$. For SPPs in lossless isotropic media, the localization length is determined by $\mathrm{Im}(\alpha)=\mathrm{Im}\sqrt{\varepsilon(\omega/c)^2-k_y^2}$. On the other hand, the localization length of a skin mode is determined by the difference of two wave vectors $\mathrm{Im}(qk_y)$. Finally, the localization side of a skin mode in uniform media depends on the propagation direction. If a skin mode propagating toward $+k_y$ is localized at the right (left) side of a system, a skin mode propagating toward $-k_y$ is localized at the left (right) side of a system [11,13,14,23].

B. Classification of dielectric tensor

The existence of the NHSE in uniform media is basically governed by the gauge potential parameter q. If q has an imaginary component, this potentially leads to the NHSE. Equation (7) tells us that this condition is fully determined by the dielectric tensor and might be satisfied for a wide variety of anisotropic media with gain or loss. Hence, here we investigate the dielectric tensor and clarify in which class of non-Hermitian anisotropic uniform media the NHSE cannot occur.

First of all, it is clear from the definition of q that the NHSE vanishes when ε is diagonal because of $q = 0$. This means the NHSE requires some type of anisotropy; in other words, some class of symmetry should be broken. It is also obvious that the NHSE cannot occur when ε is antisymmetric. Antisymmetric dielectric tensors generally appear for materials exhibiting simple circular dichroism or magneto-optical effects. Thus, NHSE cannot occur for materials showing circular dichroism or magneto-optical effect without further anisotropy.

We next discuss two internal symmetries: Lorentz reciprocity and time-reversal symmetry. Non-Hermitian systems can be classified into three classes according to the Lorentz reciprocity and time-reversal symmetry [50–52]. Non-Hermitian systems with the Lorentz reciprocity are described by complex symmetric tensors with $\varepsilon_{yx} = \varepsilon_{xy}$. The presence of the reciprocity simply modifies the definition of q as $q = \varepsilon_{xy}/\varepsilon_{xx}$ and reduces $\eta_{xx} - q^2\eta_{yy}$ to $1/\varepsilon_{xx}$. Therefore, the NHSE can occur in uniform reciprocal media if $\varepsilon_{xy}/\varepsilon_{xx}$ has nonzero imaginary component. In the case of nonreciprocal media, the NHSE can still occur when $(\varepsilon_{xy} + \varepsilon_{yx})/2\varepsilon_{xx}$ has nonzero imaginary component. Note that breaking the Lorentz reciprocity is not required for realization of the present NHSE in uniform media. Therefore, the NHSE discussed here can be realized without magneto-optical materials and by using ordinary dielectric materials and metals. This contrasts with most examples of the NHSE in discrete systems that employ nonreciprocal hopping, but reciprocal skin effects have been reported in Refs. [11,13,14,23]. Non-Hermitian systems with the time-reversal symmetry are described by real nonsymmetric tensors [51]. When ε is a real matrix, q is also real. Thus, the eigenmodes in non-Hermitian and time-reversal uniform media do not exhibit the NHSE regardless of its anisotropy.

In Sec. II A, q is represented by the xy components of the dielectric tensor. Here, we will associate q with the eigenvalue and eigenpolarizations of the dielectric tensor. We limit ourselves to dielectric tensors described by non-Hermitian normal matrices because a normal matrix is diagonalizable and the eigenvector of a normal matrix forms an orthogonal basis. We note that the definition (7) itself is valid even when the dielectric tensor is non-normal. The dielectric tensor ε is normal when it satisfies

$$|\varepsilon_{xy}| = |\varepsilon_{yx}|, \tag{21}$$

$$\varepsilon_{xy}^*(\varepsilon_{xx} - \varepsilon_{yy}) = \varepsilon_{yx}(\varepsilon_{xx}^* - \varepsilon_{yy}^*). \tag{22}$$

It is convenient to express a non-Hermitian normal matrix by

$$\varepsilon = aI + b[\sin\psi\cos\delta\sigma_x + \sin\psi\sin\delta\sigma_y + \cos\psi\sigma_z], \tag{23}$$

where $0 \leqslant \psi \leqslant \pi$, $-\pi < \delta \leqslant \pi$, σ_i are the Pauli matrices, $a = (1/2)(\varepsilon_{xx} + \varepsilon_{yy})$, and b is a complex number. Equation (23) becomes diagonal matrices when $\psi = 0$ or π, becomes symmetric matrices when $\delta = 0$ or π, and becomes antisymmetric matrices when $\delta = \pm\pi/2$. The eigenvalues $\varepsilon_{1,2}$ and corresponding eigenvectors $u_{1,2}$ of Eq. (23) are given by

$$\varepsilon_{1,2} = a \pm b, \tag{24}$$

$$u_1 = \left(\cos\frac{\psi}{2}, e^{i\delta}\sin\frac{\psi}{2}\right)^T, \tag{25}$$

$$u_2 = \left(-e^{-i\delta}\sin\frac{\psi}{2}, \cos\frac{\psi}{2}\right)^T. \tag{26}$$

The two eigenvectors generally describe two orthogonal elliptical polarizations. The angle of the long axis of the two elliptical polarizations, denoted by ϕ, is given by $\tan 2\phi = \tan\psi\cos\delta$ [53].

We particularly discuss the eigenvector of symmetric tensors and antisymmetric tensors. Non-Hermitian systems with the Lorentz reciprocity are described by complex symmetric tensors. Non-Hermitian symmetric tensors can be derived by putting $\delta = 0$ or $\delta = \pi$ in Eq. (23). The two eigenvectors are given by

$$u_1 = \left(\cos\frac{\psi}{2}, \pm\sin\frac{\psi}{2}\right)^T, \tag{27}$$

$$u_2 = \left(\mp\sin\frac{\psi}{2}, \cos\frac{\psi}{2}\right)^T. \tag{28}$$

The normal symmetric tensor describes systems where two eigenpolarizations are two orthgonal linear polarizations whose angle is $\psi/2$. Particularly, Eqs. (27) and (28) represent linearly x- and y-polarized when $\psi = 0$ or $\psi = \pi$. Next, we discuss normal antisymmetric tensors because the NHSE in uniform media does not occur in systems with antisymmetric tensors. Non-Hermitian antisymmetric tensors can be derived by putting $\delta = \pm\pi/2$ in Eq. (23). The two eigenvectors are given by

$$u_1 = \left(\cos\frac{\psi}{2}, \pm i\sin\frac{\psi}{2}\right)^T, \tag{29}$$

$$u_2 = \left(\mp i\sin\frac{\psi}{2}, \cos\frac{\psi}{2}\right)^T. \tag{30}$$

The normal antisymmetric tensor describes systems where two eigenpolarizations are orthogonal elliptical polarizations. The long axis of one elliptocal polarization is oriented along the x direction, and the long axis of the other is oriented along the y direction. Eigenpolarizations (29) and (30) particularly become two opposite circular polarizations when $\psi = \pi/2$.

A normal matrix is diagonalizable by unitary matrices. By using the unitary transformation, ε can be expressed by using $\varepsilon_{1,2}$, ψ, and δ:

$$\begin{aligned}\varepsilon &= U\begin{pmatrix}\varepsilon_1 & 0\\ 0 & \varepsilon_2\end{pmatrix}U^{-1}\\ &= \begin{pmatrix}\varepsilon_1\cos^2\frac{\psi}{2} + \varepsilon_2\sin^2\frac{\psi}{2} & (\varepsilon_1 - \varepsilon_2)e^{-i\delta}\cos\frac{\psi}{2}\sin\frac{\psi}{2}\\ (\varepsilon_1 - \varepsilon_2)e^{i\delta}\cos\frac{\psi}{2}\sin\frac{\psi}{2} & \varepsilon_1\sin^2\frac{\psi}{2} + \varepsilon_2\cos^2\frac{\psi}{2}\end{pmatrix},\end{aligned} \tag{31}$$

TABLE II. Condition that prohibits NHSE. Note that conditions (1)–(3) are valid regardless of the value of k_y, while condition (4) is valid only when k_y is real.

Condition	System	Mirror symmetry
(1) $\psi = 0$ or π	Optical axesare oriented along the x and y directions	x and y
(2) $\delta = \pm\pi/2$	Optical axes are oriented along the x and y directions	x and y
(3) $\varepsilon_1 = \varepsilon_2$	Isotropic	x and y
(4) $\arg(\varepsilon_1) = \arg(\varepsilon_2)$	Real and imaginary parts of dielectric ellipsoid have similar anisotropy	No mirror symmetry

$$U = \begin{pmatrix} \cos\frac{\psi}{2} & -e^{-i\delta}\sin\frac{\psi}{2} \\ e^{i\delta}\sin\frac{\psi}{2} & \cos\frac{\psi}{2} \end{pmatrix}. \tag{32}$$

The corresponding q is calculated as

$$q = \frac{(\varepsilon_1 - \varepsilon_2)\cos(\psi/2)\sin(\psi/2)\cos\delta}{\varepsilon_1\cos^2(\psi/2) + \varepsilon_2\sin^2(\psi/2)}. \tag{33}$$

Using this result, we summarize that NHSE cannot occur when one of the following conditions are satisfied: (1) $\psi = 0$ or π; (2) $\delta = \pm\pi/2$; and (3) $\varepsilon_1 = \varepsilon_2$. Conditions (1) and (2) mean that $q = 0$ when the long axes of two polarizations are oriented along the x and y directions. Condition (3) means that $q = 0$ when ε is isotropic. Therefore, the optical NHSE generally occurs in anisotropic media with gain or loss, including uniaxially or biaxially anisotropic crystals, when the anisotropy does not fall into these three cases. As pointed out before, anisotropy described by an antisymmetric tensor, such as circular dichroism or Faraday effect does not lead to NHSE because it satisfies condition (2), though materials showing circular dichroism or magneto-optic effect can exhibit NHSE when they possess extra anisotropy destroying some of three conditions.

Finally, we separately calculate the real and imaginary parts of Eq. (33). They are given by

$$\mathrm{Re}(q) = \frac{\cos(\psi/2)\sin(\psi/2)\cos\delta}{|\varepsilon_1\cos^2(\psi/2) + \varepsilon_2\sin^2(\psi/2)|^2}\Bigg[\{|\varepsilon_1|^2 - \mathrm{Re}(\varepsilon_1^*\varepsilon_2)\} \times \cos^2\frac{\psi}{2} - \{|\varepsilon_2|^2 - \mathrm{Re}(\varepsilon_1^*\varepsilon_2)\}\sin^2\frac{\psi}{2}\Bigg], \tag{34}$$

$$\mathrm{Im}(q) = \frac{\cos(\psi/2)\sin(\psi/2)\cos\delta}{|\varepsilon_1\cos^2(\psi/2) + \varepsilon_2\sin^2(\psi/2)|^2}\mathrm{Im}(\varepsilon_1\varepsilon_2^*). \tag{35}$$

The real and imaginary parts are generally finite. However, they sometimes accidentally vanish. Equation (34) vanishes when the terms in the square brackets vanish [see Figs. 1(g) and 1(h)]. Equation (35) vanishes when $\arg(\varepsilon_1) = \arg(\varepsilon_2)$ (mod π). When k_y is real, NHSE is inhibited when $\mathrm{Im}(q) = 0$. Equation (35) means that there appears an additional inhibition condition of NHSE, that is, $\arg(\varepsilon_1) = \arg(\varepsilon_2)$ (mod π). In other words, when the real and imaginary parts of the dielectric ellipsoid have similar anisotropy, such anisotropy does not lead to NHSE. The condition that prohibits the NHSE is summarized in Table II. An example of this case is shown in Figs. 1(e) and 1(f).

C. Numerical results

In order to visualize some of conclusions derived from the theory, we present some numerical results of non-Hermitian anisotropic media. We first consider a reciprocal and lossy anisotropic medium. Based on our previous results, this uniform medium should show NHSE. The calculated eigenfrequency ω_{PBC} is plotted in Fig. 1(a). The isofrequency contours of $\mathrm{Re}(\omega_{\mathrm{PBC}})$ and $\mathrm{Im}(\omega_{\mathrm{PBC}})$ form ellipsoids tilted from the x and y axes. The inclination of the isofrequency contour reflects the shift of the wave vector caused by the real part of the effective gauge potential and reflects the asymmmetry of the system in the x direction. Figure 1(b) shows calculated ω_{PBC} and ω_{PEC} when $k_yL/2\pi = 0$ and $k_yL/2\pi = \pm3$. The trajectories of ω_{PBC} and ω_{PEC} on the complex-ω plane are different when $k_y \neq 0$. The trajectory of ω_{PEC} is inside the open arc drawn by ω_{PBC} when $k_y \neq 0$. The shape of the trajectory of ω_{PBC} is the same at k_y and $-k_y$. However, the winding of the trajectory of ω_{PBC} when k_x increases is opposite to each other: In Figs. 1(b) and 1(h), the trajectory winds clockwise when $k_yL/2\pi = 3$ while winds counterclockwise when $k_yL/2\pi = -3$. The direction of the winding is related to the winding number and determined by the sign of $\mathrm{Im}(qk_y)$ (the proof is presented in Appendix C). The amplitude of the electric field at $k_yL/2\pi = 0$ and ±3 is also plotted in Fig. 1(b). When $k_y = 0$, $|E_y|$ is extended over the system. On the other hand, $|E_y|$ is localized at the left (right) boundary when $k_yL/2\pi = 3$ ($k_yL/2\pi = -3$) because of $\mathrm{Im}(qk_y) > 0$ [$\mathrm{Im}(qk_y) < 0$]. The localization length of the envelope of $|E_y|$ in Fig. 1(b) is accurately described by the analytical $|\mathrm{Im}(qk_y)|^{-1}$. Note that the position of the skin mode is determined by the winding direction, which is the same as the topological property of the NHSE in periodic systems.

As a second example, Figs. 1(c) and 1(d) show the numerical results when the dielectric tensor is antisymmetric. Based on our previous analysis, this uniform medium should not show NHSE. In this case, the isofrequency contour of ω_{PBC} is symmetric with respect to $k_x = 0$ and $k_y = 0$ [Fig. 1(c)]. We can see that the trajectories of ω_{PBC} and ω_{PEC} agree even when $k_y \neq 0$ [Fig. 1(d)]. These numerical results visualize the disappearance of the NHSE in systems with antisymmetric tensors.

As a third example, the NHSE in uniform media also vanishes when $\mathrm{Im}(qk_y) = 0$. Figure 1(e) shows the isofrequency contour of ω_{PBC} for the case of $\arg(\varepsilon_{xx}) = \arg(\varepsilon_{xy} + \varepsilon_{yx})$. The isofrequency contours of ω_{PBC} are tilted by the real effective gauge potential. However, both $\mathrm{Re}(\omega_{\mathrm{PBC}})$ and $\mathrm{Im}(\omega_{\mathrm{PBC}})$ become symmetric with respect to $k_x + qk_y = 0$ when q is real [see Eq. (6)]. The trajectories of ω_{PBC} and ω_{PEC} agree even when $k_y \neq 0$, as shown in Fig. 1(f). Thus, this medium does not show NHSE. In this particular case, although the system lacks the mirror symmetry with respect to the yz plane, the NHSE accidentally vanishes when both q and k_y are real. We note that $\mathrm{Im}(q) = 0$, such as Figs. 1(e) and 1(f), is a

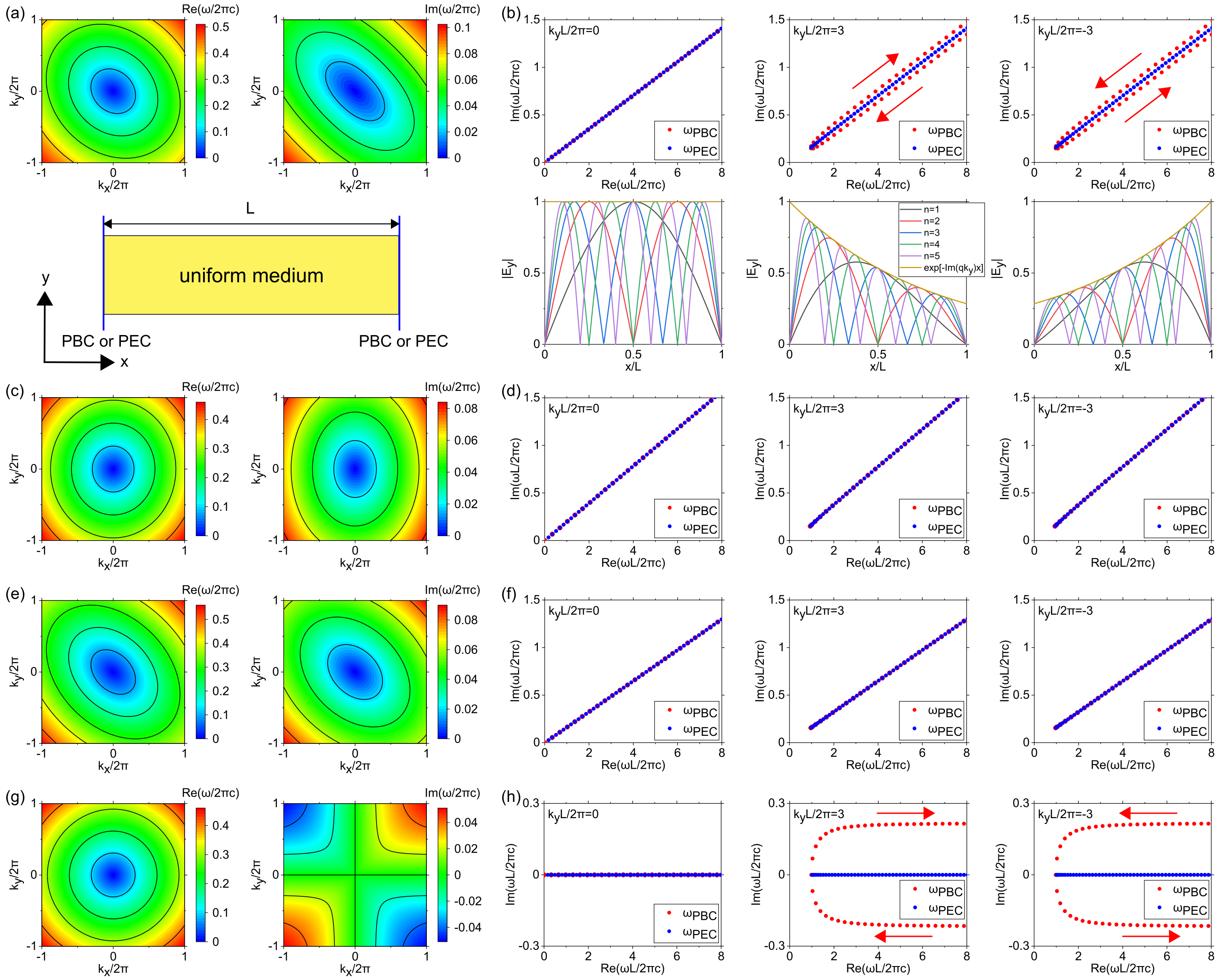

FIG. 1. (a), (c), (e), (g) Calculated (left) $\mathrm{Re}(\omega_{\mathrm{PBC}})$ and (right) $\mathrm{Im}(\omega_{\mathrm{PBC}})$ in the limit of $L \to \infty$ as functions of k_x and k_y. Lower panel of (a) is a schematic illustration of a system. (b), (d), (f), (h) Calculated complex ω_{PBC} and ω_{PEC} at (left) $k_yL/2\pi = 0$, (middle) 3, and (right) -3 on the complex-ω plane. Red arrows represent the direction of the trajectory when k_x increases. Lower panels of (b) plot $|E_y|$ calculated from Eq. (17) when $k_yL/2\pi = 0$ and $k_yL/2\pi = \pm 3$. The used value of the dielectric tensor and the corresponding q are as follows: (a), (b) $\varepsilon_{xx} = \varepsilon_{yy} = 9 - 3i$, $\varepsilon_{xy} = \varepsilon_{yx} = 2$, and $q = 0.2 + (1/15)i$. (c), (d) $\varepsilon_{xx} = 10 - 3i$, $\varepsilon_{yy} = 8 - 3i$, $\varepsilon_{xy} = 2i$, $\varepsilon_{yx} = -2i$, and $q = 0$. (e), (f) $\varepsilon_{xx} = \varepsilon_{yy} = 9 - 3i$, $\varepsilon_{xy} = \varepsilon_{yx} = 3 - i$, and $q = 0$. (g), (h) $\varepsilon_{xx} = \varepsilon_{yy} = 9$, $\varepsilon_{xy} = \varepsilon_{yx} = 2i$, and $q = 2i/9$.

transition point between $\mathrm{Im}(q) > 0$ and $\mathrm{Im}(q) < 0$. By introducing perturbation of the anisotropy that switches the sign of $\mathrm{Im}(q)$, we can switch the localization side of the skin mode if k_y is real.

Finally, we discuss a system with mirror-time symmetry, which corresponds to gain-loss balanced anisotropic media. If the diagonal components of ε are real and the off-diagonal components are pure imaginary, a system is mirror-time symmetric. The detailed discussion of the mirror-time symmetry is given in Appendix D. Based on our previous results, this medium should show NHSE. Figure 1(g) shows that $\mathrm{Re}(\omega_{\mathrm{PBC}})$ is symmetric with respect to $k_x = 0$ and $k_y = 0$ and that $\mathrm{Im}(\omega_{\mathrm{PBC}})$ is antisymmetric with respect to $k_x = 0$ and $k_y = 0$. The trajectory of ω_{PEC} is located inside the open arc drawn by ω_{PBC} when $k_y \neq 0$. It should be noted that the skin mode has a real (or pure imaginary) ω_{PEC} in systems with the mirror-time symmetry because the mirror-time symmetry ensures the reality of ω_{PEC}^2.

These numerical results visualize what type of anisotropy is required to show NHSE in media with gain or loss. The anisotropy should not have the mirror symmetry in the x and y axes, and the anisotropy of $\mathrm{Re}(\omega)$ and $\mathrm{Im}(\omega)$ should be different. Such anisotropy can be realized in uniaxially or biaxially anisotropic materials with gain or loss.

III. NON-HERMITIAN SKIN EFFECT IN MULTILAYER METAMATERIAL

A. Effective medium theory

We apply our framework of the NHSE in uniform media to metamaterials with subwavelength artificial structures. To implement the anisotropy of a dielectric tensor, we adopt multilayer metamaterials consisting of two alternating layers with subwavelength thickness. We choose one layer as a dielectric layer and the other layer as a metallic layer. A metallic layer naturally leads to material loss, and a metal-insulator multilayer exhibits strong in-plane anisotropy [55,56]. The multilayer metamaterial is characterized by the period a and filling factor of a metallic layer f. When the operation wavelength is sufficiently long compared to the period of the multilayer, the multilayer can be regarded as a uniform material with a longitudinal component $\varepsilon_{\parallel}$ and a transverse component $\varepsilon_{\perp}$, as shown in Fig. 2(a). The effective permittivities are given by

$$\varepsilon_{\parallel} = f\varepsilon_1 + (1-f)\varepsilon_2, \quad \varepsilon_{\perp} = \frac{\varepsilon_1\varepsilon_2}{(1-f)\varepsilon_1 + f\varepsilon_2}. \tag{36}$$

In this paper, we consider a multilayer consisting of Cr and air. The effective permittivity of the Cr-air multilayer is shown in Fig. 2(b). The effective permittivity satisfies $\mathrm{Re}(\varepsilon_{\parallel}) < 0$ and $\mathrm{Re}(\varepsilon_{\perp}) > 0$ in a wide range of f. The imaginary part of $\varepsilon_{\parallel}$ is larger than the imaginary part of $\varepsilon_{\perp}$ in a wide range of f. The off-diagonal component of the dielectric tensor can be introduced by tilting the multilayer. By rotating the coordinate system, we derive the effective dielectric tensor of the tilted multilayer metamaterial:

$$\varepsilon = \begin{pmatrix} \varepsilon_{\perp}\cos^2\theta + \varepsilon_{\parallel}\sin^2\theta & (\varepsilon_{\perp} - \varepsilon_{\parallel})\cos\theta\sin\theta \\ (\varepsilon_{\perp} - \varepsilon_{\parallel})\cos\theta\sin\theta & \varepsilon_{\parallel}\cos^2\theta + \varepsilon_{\perp}\sin^2\theta \end{pmatrix}. \tag{37}$$

We plot the numerical result of q as functions of f and θ in Fig. 2(c). In the Cr-Air multilayer, the real and imaginary parts of q are generally finite, and q can be tuned by the filling factor and angle of the multilayer. The signs of $\mathrm{Re}(q)$ and $\mathrm{Im}(q)$ are different from each other in this case. The parameter q is symmetric with respect to $f = 0.5$ and antisymmetric with respect to $\theta = 90^\circ$. The largest $\mathrm{Im}(q)$ is achieved near $f = 0.5$ and $\theta = 16.5^\circ$. At $f = 0.5$ and $\theta = 16.5^\circ$, the value of q is $-0.7842 + 1.7407i$. The value of $|\varepsilon_{xx}|$ is plotted in Fig 2. The large value of q roughly corresponds to the small value of $|\varepsilon_{xx}|$. Figure 2(e) plots the corresponding localization length when $k_y = 0.2(2\pi/\lambda_0)$ with $\lambda_0 = 1500$ nm. The localization length can be widely tuned by f and θ. The localization length at $f = 0.5$ and $\theta = 16.5^\circ$ is approximately estimated at $|\mathrm{Im}(qk_y)|^{-1} = 0.6857$ μm when $k_y = 0.2(2\pi/\lambda_0)$.

B. Numerical results with effective medium theory and finite element method

Next, we compare the result of a multilayer with that of a corresponding effective medium. The eigenfrequency and mode profile of the Cr-Air multilayer are calculated by using finite element method in COMSOL Multiphysical 5.6. The eigenfrequencies of the effective medium and the multilayer under the PBC and PEC boundary condition are plotted in Fig. 3(a). The eigenfrequencies ω_{PBC} and ω_{PEC} of the multilayer are in good agreement with those of the effective medium when the mode index n is sufficiently small. We can observe that the trajectory of ω_{PEC} is inside the trajectory of ω_{PBC} even in the multilayer. The numerical results for metamaterials start to deviate from those for analytical uniform media at high frequencies. This deviation is reasonable because the effective medium theory should be invalid at high frequencies when the layer period is comparable to or larger than the wavelength of light. At higher frequencies, metamaterials should be considered as one- or two-dimensional photonic crystals. With this argument, the NHSE for uniform media should be adiabatically connected to the long-wavelength limit of the NHSE in the first band of photonic crystals [11–15].

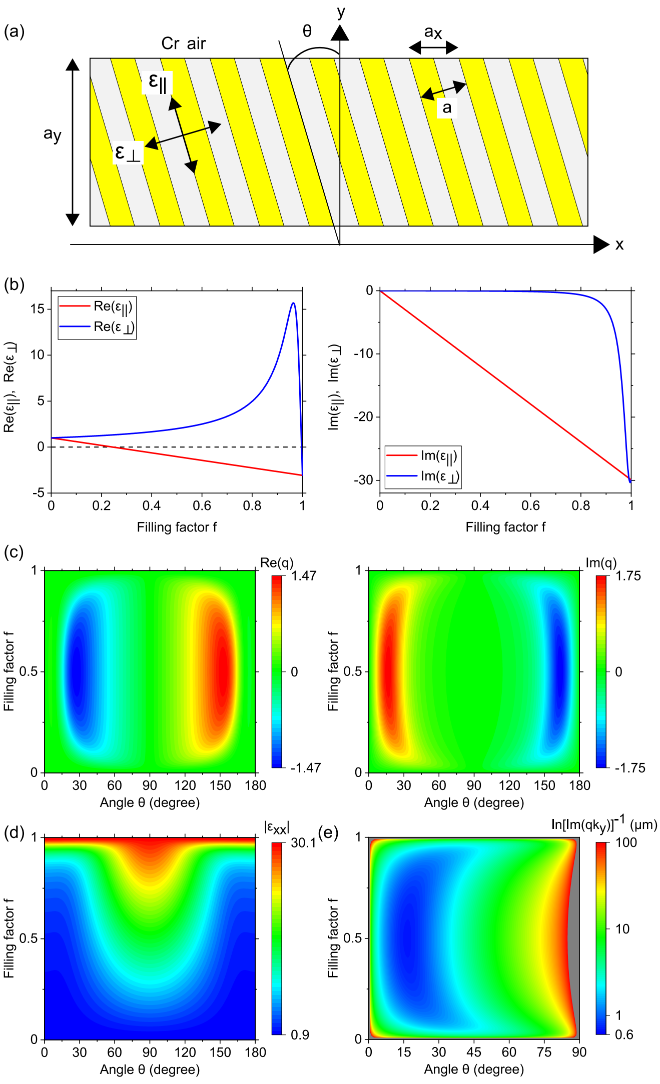

FIG. 2. (a) Schematics of a tilted multilayer metamaterial with $f = 0.5$ and $\theta = 16.5^\circ$. The period of the multilayer is denoted as a, and the tilted angle is denoted as θ. The multilayer is periodic in the x direction and y direction. The period in the x direction is given by $a_x = a/\cos\theta$, and the period in the y direction is given by $a_y = a/\sin\theta$. The structure is uniform in the z direction. (b) Numerical results of (left) $\varepsilon_{\parallel}$ and (right) $\varepsilon_{\perp}$ as a function of f. The permittivity of Cr is assumed to be $\varepsilon_{\mathrm{Cr}} = \varepsilon_1 = -3.072 - 29.929i$, which is the value at 1500 nm. The permittivity of air is $\varepsilon_{\mathrm{air}} = \varepsilon_2 = 1$. (c) Numerical result of (left) $\mathrm{Re}(q)$ and (right) $\mathrm{Im}(q)$ as functions of θ and f. (d) Numerical result of $|\varepsilon_{xx}|$. (e) Numerical result of $|\mathrm{Im}(qk_y)|^{-1}$ at $k_y = 0.2(2\pi/\lambda_0)$ as a function of θ and f with $\lambda_0 = 1500$ nm [54]. The gray regions represent regions where $|\mathrm{Im}(qk_y)|^{-1}$ is over 100 μm.

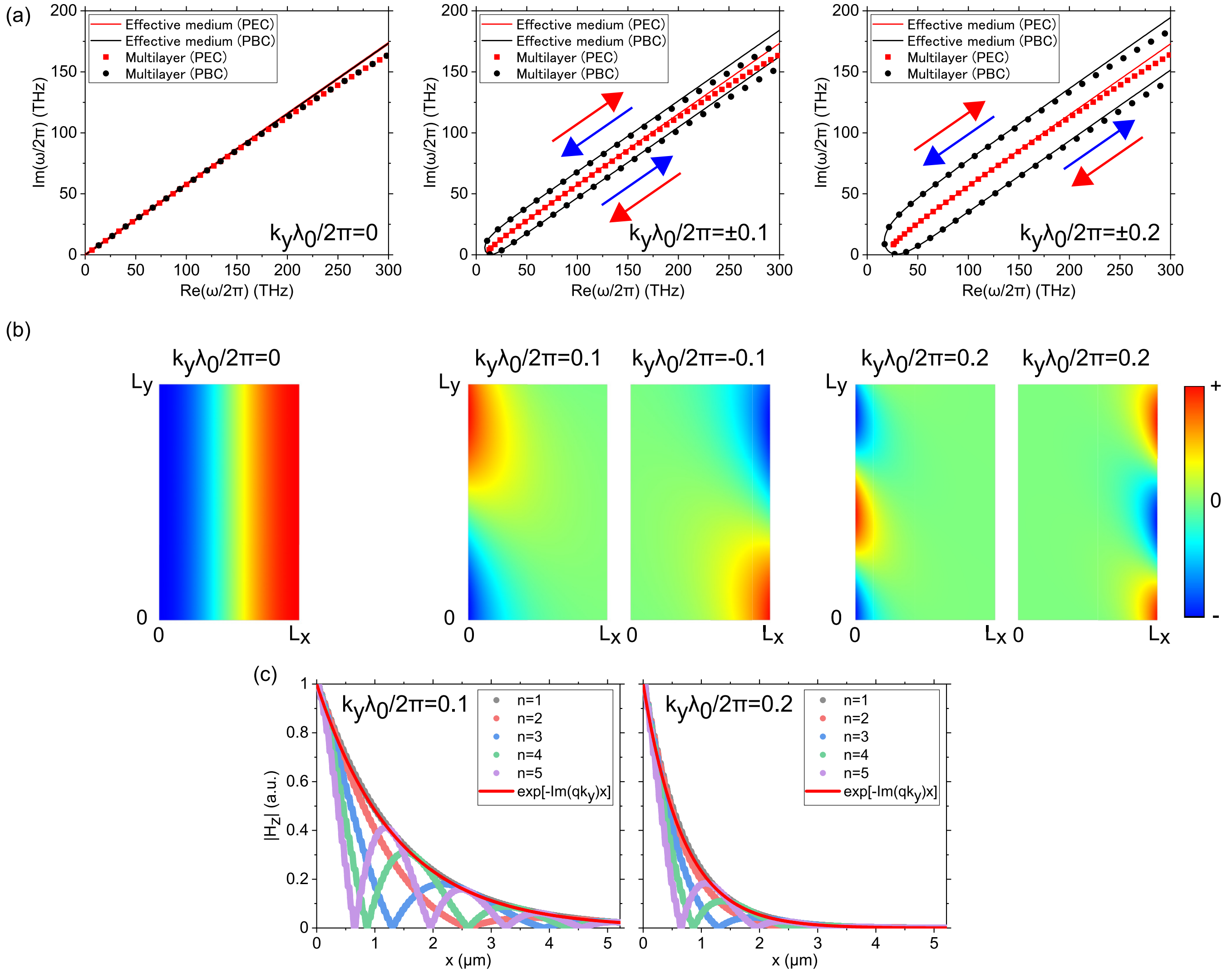

FIG. 3. (a) Trajectory of the eigenfrequencies of the effective uniform medium and multilayer when $k_y\lambda_0/2\pi = 0$ (left), ±0.1 (middle), and ±0.2 (right), where $\lambda_0 = 1500$ nm is the reference wavelength. The period of the multilayer a is set to 50 nm. The size of the system in the x direction is $L_x = 100a_x$. Red and blue arrows represent the direction of the trajectory when k_x increases. Red arrows correspond to $k_y > 0$ and blue arrows correspond to $k_y < 0$. (b) Numerical results of the eigenmode in the multilayer. The magnetic fields $H_z(x, y)$ of the lowest mode ($n = 1$) under the PEC boundary condition at $k_y\lambda_0/2\pi = 0$, ±0.1, and ±0.2 are plotted. We impose the Bloch boundary condition in the y direction and $H_z(x, y)$ satisfies $H_z(x, y + a_y) = e^{-ik_y a_y} H_z(x, y)$. The mode profile in the range from $y = 0$ to $y = L_y$ is plotted with $L_y = 500a_y$. (c) Calculated $|H_z|$ of the multilayer at (left) $k_y\lambda_0/2\pi = 0.1$ and (right) 0.2. For comparison, $\exp[-\mathrm{Im}(qk_y)]$ for (left) $k_y\lambda_0/2\pi = 0.1$ and (right) 0.2 is also plotted. The filling factor f and angle θ are set to $f = 0.5$ and $\theta = 16.5^\circ$. The values of the effective dielectric tensor are $\varepsilon_{xx} = 1.759 - 1.268i$, $\varepsilon_{yy} = -0.791 - 13.763i$, and $\varepsilon_{xy} = \varepsilon_{yx} = 0.828 + 4.057i$.

The lowest eigenmodes with $n = 1$–5 of the multilayer under the PEC boundary condition are plotted in Fig. 3(b). The magnetic field $H_z(x, y)$ at $k_y\lambda_0/2\pi = 0$ is extended over the system, while $H_z(x, y)$ is localized at the left (right) boundary when $k_y > 0$ ($k_y < 0$). The numerical result of $|H_z(x)|$ of the multilayer is shown in Fig. 3(c). The envelope of $|H_z(x)|$ in the multilayer decays exponentially in the x direction, and the envelope agrees with $\exp[-\mathrm{Im}(qk_y)]$ predicted by the effective medium theory. The localization length in the x direction $|\mathrm{Im}(qk_y)|^{-1}$ is estimated at $|\mathrm{Im}(qk_y)|^{-1} = 1.3741$ μm when $k_y\lambda_0/2\pi = 0.1$ and $|\mathrm{Im}(qk_y)|^{-1} = 0.6857$ μm when $k_y\lambda_0/2\pi = 0.2$. The skin mode is strongly localized in a region with a size comparable to the wavelength.

The results presented in this section demonstrate that one can design metamaterials showing NHSE, which is essentially similar to the NHSE in uniform media. Importantly, various characteristics of NHSE can be tuned by controlling the parameters of multilayer metamaterials. The analytical framework enables us to design NHSE in versatile ways.

IV. STATIONARILY EXCITED SKIN MODE

So far, we have discussed the skin mode with a complex ω in a parallel-plate cavity filled with a non-Hermitian anisotropic material. In the previous section, k_y is a parameter we can choose (k_y is usually taken as real), and ω is determined by k_y and n via the dispersion relation. Generally, the imaginary part of a complex frequency represents the temporal decay or amplitude of eigenmodes in a cavity, and the complex frequency is often used to describe the linewidth of a resonance. On the other hand, the parallel-plate *cavity* discussed in the previous section can also be regarded as a parallel-plate *waveguide* that extends in the y direction and is bounded in the x direction. To describe propagation loss of a waveguide mode, the wave vector is usually taken to be complex and the frequency is taken to be real. The imaginary part of the wave vector represents the spatial decay of an electromagnetic field. This choice is reasonable because the complex wave vector is adopted in many textbooks of electromagnetism to describe the propagation of waves in lossy systems [40,57,58]. The complex wave vector has been used in periodic systems to describe the propagation loss [59–62]. In two- (or three-) dimensional systems, we have to choose whether ω or k should be a complex number depending on the situation. Based on these ideas, we extend the theory of the NHSE to real-ω modes and introduce skin modes with real ω and complex k_y. For real-ω skin modes, ω is taken as a parameter we can choose, and k_y is determined by ω and n via the dispersion relation. Here, we show that the localization of an electromagnetic field occurs even under real-ω condition. More importantly, the localization length of a real-ω skin mode generally differs from that of a real-k skin mode. The distinction between a real-k skin mode and a real-ω skin mode is crucial because one may exhibit NHSE but the other may not exhibit NHSE. We note that the response of the NHSE in one-dimensional systems under stationary excitation was investigated in Refs. [63,64], especially focusing on the local density of states. In this paper, we are interested in mode profile, localization, and propagation. We note that the introduction of complex wave vector is characteristic for two- or three-dimensional systems. This method cannot be applied to the NHSE in bounded one-dimensional systems such as Hatano-Nelson model.

Before proceeding, we mention an experimental system we imagine and how to excite the stationary skin mode [see Fig. 4(a)]. To excite a real-ω skin mode, we should consider an interface between a lossless isotropic medium and a non-Hermitian anisotropic medium sandwiched by two PECs placed at $x = 0$ and $x = L$. Such discontinuity of the parallel-plate slab waveguide is usually analyzed by modal analysis [58] based on an expansion with the transverse mode numbers. When a certain incident mode in the lossless isotropic region with an excitation frequency ω is injected to the non-Hermitian anisotropic medium, it is expected that an excited wave can be written by the sum of real-ω skin modes for different transverse mode numbers with the same frequency ω. In this paper, we consider a real-ω mode with a given n. Alternatively, we can place excitation sources inside a waveguide to excite real-ω modes [see the right panel of Fig. 4(a)]. If the frequency and the distribution of a source are consistent with those of an eigenmode, its eigenmode can be selectively excited.

A. Theory

For a specific example, we reconsider a parallel-plate waveguide filled by a non-Hermitian anisotropic medium. In contrast to the previous section, we seek solutions with a real ω. The boundary condition at $x = 0$ and $x = L$ determines k_x, and k_y is derived by solving the dispersion relation for k_y as functions of ω and k_x. Under the PEC boundary condition, $k_\pm$ and k_y are given by

$$k_\pm = \pm\frac{\pi n}{L} - qk_{y,n}(\omega), \tag{38}$$

$$k_{y,n}(\omega) = \pm\sqrt{\frac{1}{\eta_{xx} - q^2\eta_{yy}}\left\{\left(\frac{\omega}{c}\right)^2 - \eta_{yy}\left(\frac{\pi n}{L}\right)^2\right\}}, \tag{39}$$

where ω is the real-valued excitation frequency and n is the transverse mode number. The real-ω mode under the PEC boundary condition can be simply derived by inserting Eq. (39) into Eqs. (17)–(19). The propagation direction is determined by the time-averaged power flow. The time-averaged Poynting vector and power flow are discussed in Appendix E. Note that $k_{y,n}$ is determined through the dispersion relation for specific n, although k_y is predetermined in the NHSE in the previous sections. This derivation shows that the stationarily excited electromagnetic modes (i.e., the real-ω modes) are expressed as the same equations as in the real-k_y modes in the previous sections, and thus they are exponentially localized near one of the boundaries when $\mathrm{Im}[qk_{y,n}(\omega)] \neq 0$. Importantly, the localization of the real-ω mode is completely characterized by $\mathrm{Im}(qk_y)$, which is also the same as in the NHSE in the real-k_y mode, and thus the localization of the real-ω mode is caused by the effective imaginary gauge potential as in the Hatano-Nelson model. Therefore, we regard that these localized modes can be considered the NHSE in the stationary excited modes.

The only difference between the real-k_y mode and real-ω mode is which quantity (k_y or ω) is forced to be real. This leads to some different characteristics between the stationarily excited NHSE with real-ω modes and the conventional NHSE with real-k_y modes. First, k_y depends on ω and n for the real-ω mode. Therefore, the localization length in the x direction of real-ω skin modes depends on ω and n via $k_{y,n}(\omega)$. Second, k_y is generally complex for the real-ω mode, and $\mathrm{Im}[k_{y,n}(\omega)]$, which represents the attenuation constant in the y direction, contributes to the localization of the real-ω skin mode because $\mathrm{Im}(qk_y)$ is written by $\mathrm{Im}(qk_y) = \mathrm{Im}(q)\mathrm{Re}(k_y) + \mathrm{Re}(q)\mathrm{Im}(k_y)$. For the real-$k_y$ skin mode, only the first term contributes to $\mathrm{Im}(qk_y)$ because k_y is real. On the other hand, both the real and imaginary parts of q play a role for the localization of the real-ω skin mode.

We derived conditions for the form of dielectric tensors that prohibit the real-k_y modes. Since the real-ω skin modes can be formed even for real q, condition (4) in Table II is relaxed. This means that the real-ω skin modes can occur in a wider range of anisotropic non-Hermitian media if we set the boundaries at an appropriate direction.

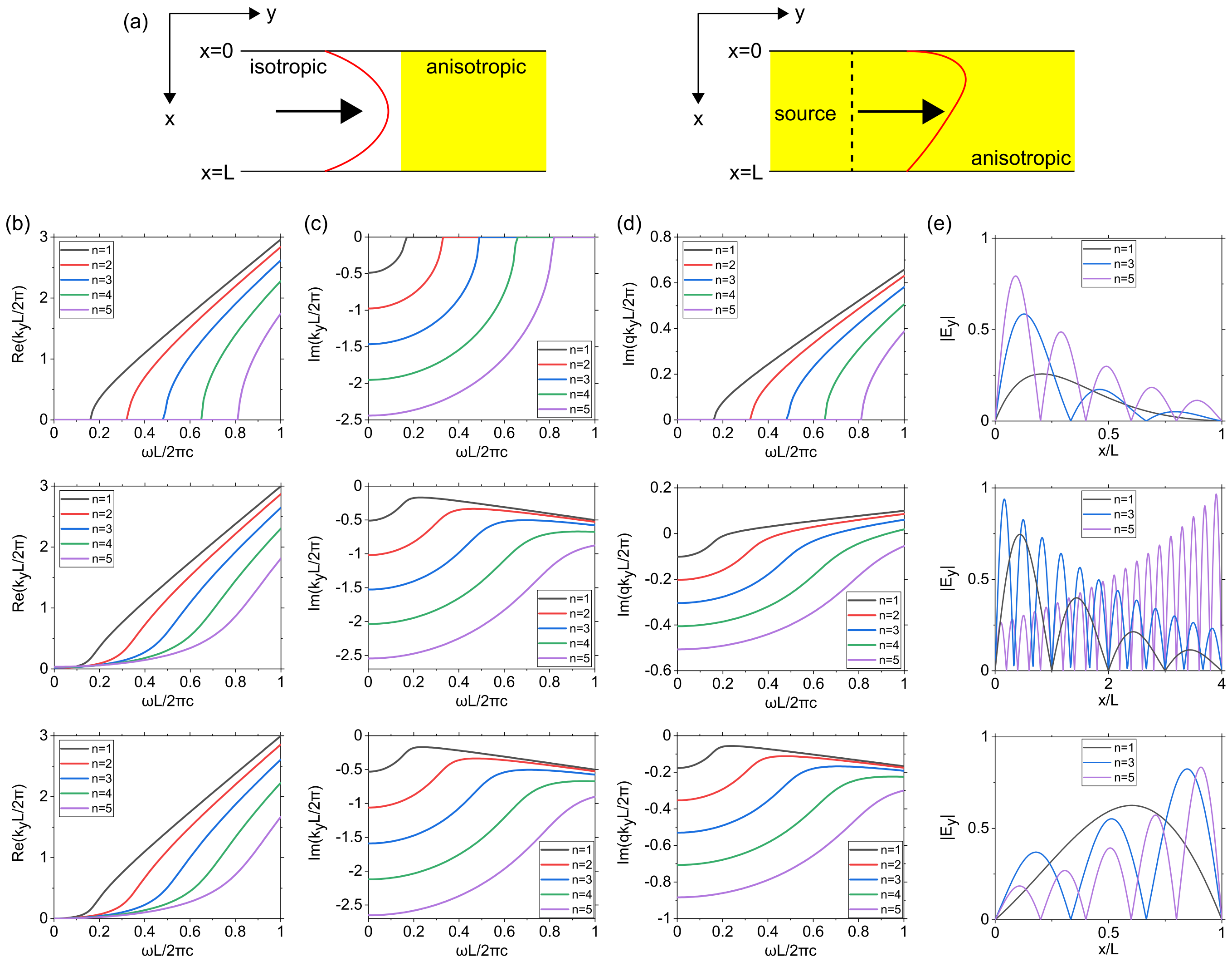

FIG. 4. Dispersion relation and localization strength of real-ω skin mode. (a) Schematic illustration of excitation of real-ω mode. Left: An electromagnetic wave is injected from an isotropic region. Right: A waveguide mode is excited by a source placed at a waveguide. Numerical result of (b) $\mathrm{Re}(k_y)$, (c) $\mathrm{Im}(k_y)$, and (d) $\mathrm{Im}(qk_y)$ for $n = 1$–5. (e) Normalized $|E_y|$ for $n = 1, 3,$ and 5. The frequency is fixed at $\omega L/2\pi c = 1$. The dielectric tensor is set to $\varepsilon_{xx} = \varepsilon_{yy} = 9$ and $\varepsilon_{xy} = \varepsilon_{yx} = 2i$ in the upper panels, $\varepsilon_{xx} = \varepsilon_{yy} = 9 - 3i$ and $\varepsilon_{xy} = \varepsilon_{yx} = 2$ in the middle panels, and $\varepsilon_{xx} = \varepsilon_{yy} = 9 - 3i$ and $\varepsilon_{xy} = \varepsilon_{yx} = 3 - i$ in the lower panels.

B. Numerical results of stationarily excited non-Hermitian skin mode

Here, we present some numerical results of the real-ω skin mode and compare it with the real-k_y skin mode. First, we begin with a special case with the mirror-time symmetry, where ω and k_y can be simultaneously real although the system is non-Hermitian. Figures 4(b) and 4(c) show the numerical result of k_y as a function of ω for several mode indexes n. In the mirror-time symmetric system, it is useful to define the cutoff frequency ω_c given by

$$\frac{\omega_c}{c} = \sqrt{(\eta_{xx} - q^2\eta_{yy})k_y^2}. \tag{40}$$

As shown in Figs. 4(b) and 4(c), k_y is real (pure imaginary) above (below) the cutoff frequency if $\eta_{yy} > 0$. Figure 4(d) plots the calculated $\mathrm{Im}(qk_y)$. This shows that even for stationarily excited modes, $\mathrm{Im}(qk_y)$ becomes nonzero when real-valued ω is higher than the cutoff frequency. The modes with $n = 1, 3,$ and 5 are plotted in Fig. 4(e). When $\varepsilon_{xx} = \varepsilon_{yy} = 9$ and $\varepsilon_{xy} = \varepsilon_{yx} = 2i$ [Fig. 4(e)], the modes with $n = 1, 3,$ and 5 are exponentially localized at left boundary. The localization length becomes longer as n increases. These localization phenomena are explained by the value of $\mathrm{Im}(qk_y)$ [see Fig. 4(d)]. The positive value of $\mathrm{Im}(qk_y)$ means the localization at the right boundary, and the larger value of $|\mathrm{Im}(qk_y)|$ means the shorter localization length. We note that the localization side may change depending on ω and n. When $\varepsilon_{xx} = \varepsilon_{yy} = 9 - 3i$ and $\varepsilon_{xy} = \varepsilon_{yx} = 2$, the modes with $n = 1$ and $n = 3$ are localized at the left boundary, while the mode with $n = 5$ is localized at the right boundary. These two modes have different localization lengths because k_y depends on n, in contrast to the real-k_y skin mode. Figures 5(a) and 5(b) show the comparison with the real-ω skin mode and real-k_y skin mode. In the case with the mirror-time symmetry, importantly, the dispersion and $\mathrm{Im}(qk_y)$ of real-ω skin modes completely coincide with those of real-k_y skin modes. We conclude that

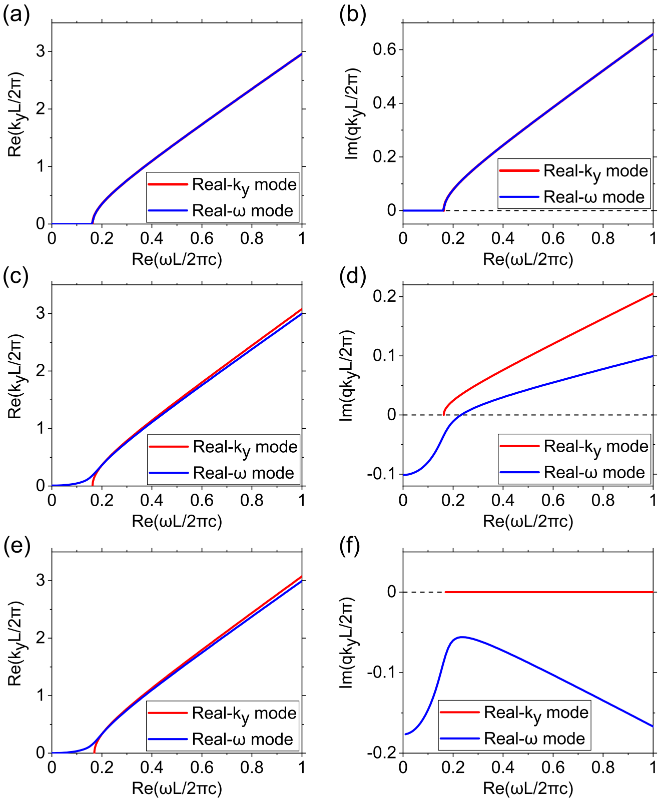

FIG. 5. Comparison between real-k_y skin mode and real-ω skin mode. (a), (c), (e) Comparison of dispersion relations between $\mathrm{Re}(k_y)$ and $\mathrm{Re}(\omega)$. (b), (d), (f) Comparison of the localization strength $\mathrm{Im}(qk_y)$ as a function of $\mathrm{Re}(\omega)$. The dielectric tensor is set to (a), (b) $\varepsilon_{xx} = \varepsilon_{yy} = 9$ and $\varepsilon_{xy} = \varepsilon_{yx} = 2i$, (c), (d) $\varepsilon_{xx} = \varepsilon_{yy} = 9 - 3i$ and $\varepsilon_{xy} = \varepsilon_{yx} = 2$, and (e), (f) $\varepsilon_{xx} = \varepsilon_{yy} = 9 - 3i$ and $\varepsilon_{xy} = \varepsilon_{yx} = 3 - i$. The mode index is fixed at $n = 1$ in all plots.

one can externally excite skin modes essentially the same as those in the previous sections, with the presence of the mirror-time symmetry.

Next, we investigate a more general situation in Figs. 4, 5(c), and 5(d). The imaginary part of k_y is negative, and thus the real-ω mode is attenuated in the y direction. We observe that $\mathrm{Im}(qk_y)$ is nonzero in the wide frequency region, proving the existence of the NHSE in this case, as shown in Figs. 4, 5(c), and 5(d). However, the dispersion relation and $\mathrm{Im}(qk_y)$ of the real-k_y mode and real-ω mode are now different from each other. We also observe that the sign of $\mathrm{Im}(qk_y)$ of the real-ω skin mode changes while sweeping ω and n [see Fig. 4(e)]. This is because $\mathrm{Re}(q)\mathrm{Im}(k_y)$ has the opposite sign of $\mathrm{Im}(q)\mathrm{Re}(k_y)$. The inversion of the sign involves the inversion of the localization position, and thus the present result demonstrates that the real-ω skin mode exhibits different localization in the x direction compared to the real-k_y mode.

Finally, we show another special case with real q in Figs. 4, 5(e), and 5(f). As shown in Figs. 1(e) and 5(f), the real-k_y mode does not exhibit NHSE when q is purely real. However, we observe that $\mathrm{Im}(qk_y)$ becomes nonzero in a wide frequency range for real-ω modes. The present result shows that the localization strength $\mathrm{Im}(qk_y)$ of the real-k_y mode vanishes for all $\mathrm{Re}(\omega)$, while $\mathrm{Im}(qk_y)$ of the real-ω mode can become finite because of the imaginary part of k_y.

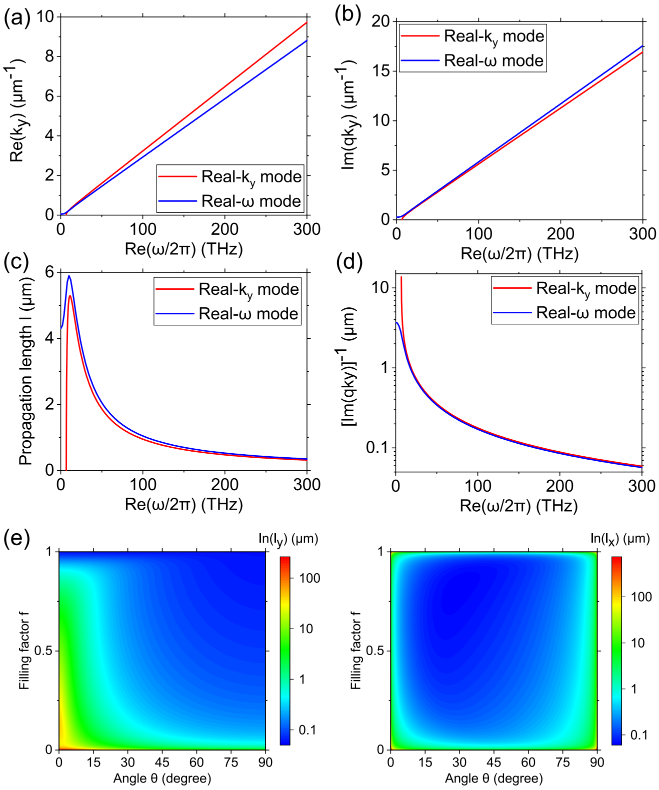

FIG. 6. Propagation and localization length of effective medium. (a) Comparison of dispersion relation of the effective medium between $\mathrm{Re}(k_y)$ and $\mathrm{Re}(\omega)$. (b) Comparison of the localization strength $\mathrm{Im}(qk_y)$ as a function of $\mathrm{Re}(\omega)$. (c) Comparison of the propagation length in the y direction calculated from real-k_y mode and real-ω mode. (d) Comparison of the localization length in the y direction calculated from real-k_y mode and real-ω mode. (e) Numerical result of propagation length in the y direction l_y and (right) localization length in the x direction l_x as functions of f and θ. The excitation wavelength is fixed at 1500 nm. In all plots, the mode index is fixed at $n = 1$.

These results show that exponentially decaying skin modes appear for stationarily excited cases (real-ω skin modes), which are caused by $\mathrm{Im}(q)$ and $\mathrm{Re}(q)$. The former generates very similar skin modes to those in eigenfunctions (real-k_y skin modes), but the latter generates skin modes that do not have counterparts in real-k_y skin modes. Interestingly, one can switch the localization position by manipulating these two different contributions, which may lead to different aspects or applications of the NHSE.

C. Estimation of propagation and localization length in multilayer metamaterial

Next, we estimate the propagation length in the y direction and localization length in the x direction in the Cr-Air multilayer by using the effective medium theory. To compare the real-ω skin mode with the real-k_y skin mode, we first set f and θ to $f = 0.5$ and $\theta = 16.5^\circ$. Figures 6(a) and 6(b) show the comparison of $\mathrm{Re}(k_y)$ and $\mathrm{Im}(qk_y)$ for the real-k_y mode and real-ω mode with $n = 1$. Figure 6(c) shows the propagation length in the y direction. For the real-k_y mode, we define the propagation length as $\mathrm{Im}(\omega_{\mathrm{PEC}})^{-1} v_g$, where $v_g = d\mathrm{Re}(\omega_{\mathrm{PEC}})/dk_y$ is the group velocity of the skin mode.

For the real-ω mode, the propagation length is calculated by $|\mathrm{Im}(k_y)|^{-1}$. When material loss or gain is sufficiently small, it is expected that the propagation lengths of the real-k_y mode and real-ω mode coincide with each other [62]. In this case, however, the propagation lengths calculated from the two modes do not agree with each other due to non-negligible material loss. At $\mathrm{Re}(\omega/2\pi) \approx 200$ THz, the propagation length of the real-k_y mode is about 476 nm, while the propagation length of the real-ω mode is about 527 nm. The numerical result of the localization length in the x direction is plotted in Fig. 6(d). In the effective medium of the multilayer, only small difference appears. At $\mathrm{Re}(\omega/2\pi) \approx 200$ THz, the localization length of the real-k_y mode is about 88.5 nm, while the localization length of the real-ω mode is about 85.5 nm.

Finally, we estimate the propagation length l_y of the real-ω skin mode and localization length l_x of the real-ω skin mode as functions of f and θ. The excitation wavelength is fixed at 1500 nm, and the mode index n is fixed at 1. The numerical result of the propagation length is shown in Fig. 6(e). Smaller f enhances the propagation length because the material loss can be reduced by reducing the volume of the metallic Cr layer. In addition, smaller θ enhances the propagation length because $\varepsilon_\perp$ becomes more dominant than $\varepsilon_\parallel$ as θ becomes smaller. In regions where f and θ are small, the propagation length reaches several micrometers. Figure 6(e) also shows the numerical calculation of the localization length. For the real-k_y mode, the strongest localization is achieved near $f = 0.5$ and $\theta = 16.5^\circ$ [Fig. 2(c)], while the strongest localization is achieved near $f = 0.82$ and $\theta = 29.5^\circ$ for the real-ω mode with excitation wavelength 1500 nm and $n = 1$. This deviation is caused by the imaginary part of k_y. The localization length of the real-ω mode is less than 1 μm in the wide range of f and θ, which indicates that the real-ω skin mode is localized in a region as small as the operation wavelength.

V. DISCUSSION AND CONCLUSION

In summary, we theoretically demonstrate that the optical NHSE occurs in non-Hermitian anisotropic media. The localization occurs when $\mathrm{Im}(qk_y) \neq 0$, and its localization length in the x direction is given by $|\mathrm{Im}(qk_y)|^{-1}$. A skin mode propagating in the $+y$ direction is localized at a boundary of a system, while the counterpropagating skin mode is localized at the opposite boundary. This peculiar localization arises from the combination of the non-Hermiticity and anisotropy. At a glance, it seems that this phenomenon is nonreciprocal like topological edge modes in photonic Chern insulators without time-reversal symmetry [65–68]. However, the propagation of the skin mode discussed in this paper is essentially reciprocal because the NHSE occurs even when ε is symmetric. The advantage of using uniform media is that the NHSE in uniform media can be analytically predicted. The NHSE also occurs in photonic crystals with appropriate structure and dielectric permittivity. However, we cannot predict the strength of the localization in photonic crystals without detailed numerical calculations. On the other hand, the NHSE in uniform media is completely governed by a dielectric tensor. Because a dielectric tensor can be tuned by external fields, the NHSE in uniform media also may be controlled by external fields. We also show the existence of the NHSE in the multilayer metamaterials. We finally propose a concept of a stationarily excited skin mode. Interestingly, in non-Hermitian anisotropic media, the spatial distribution of an eigenmode differs from that of an excited mode in contrast to Hermitian systems. The notion of a stationarily excited skin mode can be extended to two-dimensional periodic crystals by using the complex-k band method [57–60]. We expect that the NHSE with real ω and complex k_y can be realized by exciting like Fig. 4(a). The system size in the y direction needs to be longer than the propagation length.

Our theory presents the simplest model of the optical NHSE, and it is useful for a better understanding of NHSE. In addition, our theory allows us to implement optical NHSE in a wider variety of systems, such as metamaterials described by effective dielectric approximation and anisotropic materials in nature. The limitation is that our model has no band gap. Previous works discussed the competition between bulk skin modes and edge states within a band gap [12]. This phenomenon cannot be observed in our model. In addition, our model is always twofold rotational symmetric because dielectric tensor (1) is always twofold rotational symmetric, which results in that the dispersion relation is always symmetric with respect to k_y in contrast to photonic crystals [11]. Our findings can be applied to other classical wave systems; for example, the anisotropy of the elasticity tensor will lead to the NHSE for elastic waves [35,69]. Our work also paves the way to realize the optical NHSE in homogeneous materials such as bulk materials and metamaterials.

ACKNOWLEDGMENTS

This work was supported by JSPS KAKENHI (Grants No. JP20H05641, No. JP21K14551, No. JP22K18687, No. JP22H00108, and No. JP21J01409), JST PRESTO (Grant No. JPMJPR18L9), and MEXT Initiative to Establish Next-generation Novel Integrated Circuits Centers (X-NICS) (Grant No. JPJ011438).

DATA AVAILABILITY

The data that support the findings of this article are not publicly available. The data are available from the authors upon reasonable request.

APPENDIX A: RELATION BETWEEN ω_{PBC} AND ω_{PEC} ON THE COMPLEX-ω^2 PLANE

1. Trajectory of ω_{PBC} and ω_{PEC} on the complex-ω^2 plane

In the limit of $L \to \infty$, ω_{PEC} is expressed by

$$\left(\frac{\omega_{\mathrm{PEC}}}{c}\right)^2 = \eta_{yy}s^2 + (\eta_{xx} - q^2\eta_{yy})k_y^2, \tag{A1}$$

where s is the positive real number. For simplicity, we define $\lambda_{\mathrm{PEC}} = (\omega_{\mathrm{PEC}}/c)^2 - (\eta_{xx} - q^2\eta_{yy})k_y^2$. The real and imaginary parts of λ_{PEC} are given by

$$\mathrm{Re}(\lambda_{\mathrm{PEC}}) = \mathrm{Re}(\eta_{yy})s^2, \quad \mathrm{Im}(\lambda_{\mathrm{PEC}}) = \mathrm{Im}(\eta_{yy})s^2. \tag{A2}$$

By eliminating s, we obtain

$$\mathrm{Im}(\lambda_{\mathrm{PEC}}) = \frac{\mathrm{Im}(\eta_{yy})}{\mathrm{Re}(\eta_{yy})}\mathrm{Re}(\lambda_{\mathrm{PEC}}). \tag{A3}$$

The trajectory of ω_{PEC}^2 is a semi-infinite line on the complex-ω^2 plane, and its inclination is given by $\mathrm{Im}(\eta_{yy})/\mathrm{Re}(\eta_{yy})$.

Similarly, in the limit of $L \to \infty$, ω_{PBC} is expressed by

$$\left(\frac{\omega_{\mathrm{PBC}}}{c}\right)^2 = \eta_{yy}(k_x + qk_y)^2 + (\eta_{xx} - q^2\eta_{yy})k_y^2, \tag{A4}$$

where k_x is the real number. Here, we define $\lambda_{\mathrm{PBC}} = (\omega_{\mathrm{PBC}}/c)^2 - (\eta_{xx} - q^2\eta_{yy})k_y^2$ for simplicity. Defining $t = k_x + \mathrm{Re}(qk_y)$ yields

$$\lambda_{\mathrm{PBC}} = \eta_{yy}[t + i\mathrm{Im}(qk_y)]^2. \tag{A5}$$

The real and imaginary parts of λ_{PBC} are given by

$$\mathrm{Re}(\lambda_{\mathrm{PBC}}) = \mathrm{Re}(\eta_{yy})[t^2 - \{\mathrm{Im}(qk_y)\}^2] - 2\mathrm{Im}(\eta_{yy})\mathrm{Im}(qk_y)t, \tag{A6}$$

$$\mathrm{Im}(\lambda_{\mathrm{PBC}}) = \mathrm{Im}(\eta_{yy})[t^2 - \{\mathrm{Im}(qk_y)\}^2] + 2\mathrm{Re}(\eta_{yy})\mathrm{Im}(qk_y)t. \tag{A7}$$

Next, we perform a rotational coordinate transformation. We define λ_1 and λ_2 as

$$\begin{pmatrix}\lambda_1\\ \lambda_2\end{pmatrix} = \frac{1}{|\eta_{yy}|}\begin{pmatrix}\mathrm{Re}(\eta_{yy}) & \mathrm{Im}(\eta_{yy})\\ -\mathrm{Im}(\eta_{yy}) & \mathrm{Re}(\eta_{yy})\end{pmatrix}\begin{pmatrix}\mathrm{Re}(\lambda_{\mathrm{PBC}})\\ \mathrm{Im}(\lambda_{\mathrm{PBC}})\end{pmatrix}. \tag{A8}$$

$\lambda_{1,2}$ are calculated as

$$\lambda_1 = |\eta_{yy}|[t^2 - \{\mathrm{Im}(qk_y)\}^2], \tag{A9}$$

$$\lambda_2 = 2|\eta_{yy}|\mathrm{Im}(qk_y)t. \tag{A10}$$

Eliminating t, we can derive the relation between λ_1 and λ_2 for $\mathrm{Im}(qk_y) \neq 0$,

$$\lambda_1 = \frac{\lambda_2^2}{4|\eta_{yy}|\{\mathrm{Im}(qk_y)\}^2} - |\eta_{yy}|\{\mathrm{Im}(qk_y)\}^2. \tag{A11}$$

Therefore, the trajectory of ω_{PBC}^2 is a parabola when $\mathrm{Im}(qk_y) \neq 0$, while the trajectory of ω_{PBC} becomes a semi-infinite line when $\mathrm{Im}(qk_y) = 0$. The sign of $\mathrm{Im}(qk_y)$ determines the direction of the trajectory of a parabola when t increases, as illustrated in Fig. 7(a).

2. Middle-point theorem

In this section, we will prove that the trajectory of ω_{PEC}^2 is inside an open arc drawn by ω_{PBC}^2. Let us consider ω_{PBC}^2 at $k_x = k_{1,2} = \pm\sqrt{s_0^2 + \{\mathrm{Im}(qk_y)\}^2} - \mathrm{Re}(qk_y)$ with a positive real s_0. They are given by

$$\left(\frac{\omega_{\mathrm{PBC}}(k_{1,2}, k_y)}{c}\right)^2 = \eta_{yy}\left[s_0^2 \pm 2i\mathrm{Im}(qk_y)\sqrt{s_0^2 + \{\mathrm{Im}(qk_y)\}^2}\right] + (\eta_{xx} - q^2\eta_{yy})k_y^2. \tag{A12}$$

The average of them is

$$\begin{aligned}\frac{1}{2}\left[\left(\frac{\omega_{\mathrm{PBC}}(k_1, k_y)}{c}\right)^2 + \left(\frac{\omega_{\mathrm{PBC}}(k_2, k_y)}{c}\right)^2\right] &= \eta_{yy}s_0^2 + (\eta_{xx} - q^2\eta_{yy})k_y^2\\ &= \left(\frac{\omega_{\mathrm{PEC}}(s_0, k_y)}{c}\right)^2.\end{aligned} \tag{A13}$$

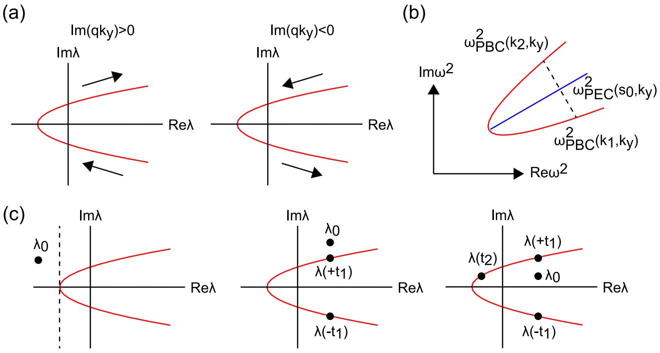

FIG. 7. (a) Schematic illustration of parabolas. Black arrows represent the direction of parabolas when t increases. (b) Schematic illustration of the trajectory of ω_{PBC}^2 and ω_{PEC}^2 on the complex-ω^2 plane. Red (blue) line represents the trajectory of ω_{PBC}^2 (ω_{PEC}^2). (c) Schematic illustration of various positions of λ_0. Broken line represents $\mathrm{Re}(\lambda) = -|\eta_{yy}|\{\mathrm{Im}(qk_y)\}^2$. In the left and middle panels, λ_0 is located outside a parabola, while λ_0 is located inside a parabola in the right panel.

Equation (A13) shows that $\omega_{\mathrm{PEC}}(s_0, k_y)$ lies at the midpoint between $\omega_{\mathrm{PBC}}(k_1, k_y)$ and $\omega_{\mathrm{PBC}}(k_2, k_y)$ on the complex-ω^2 plane as illustrated in Fig. 7(b). If $\mathrm{Im}(qk_y) = 0$, $\omega_{\mathrm{PBC}}^2(k_1, k_y)$, $\omega_{\mathrm{PBC}}^2(k_2, k_y)$, and $\omega_{\mathrm{PEC}}^2(s_0, k_y)$ satisfy

$$\omega_{\mathrm{PBC}}^2(k_1, k_y) = \omega_{\mathrm{PBC}}^2(k_2, k_y) = \omega_{\mathrm{PEC}}^2(s_0, k_y). \tag{A14}$$

APPENDIX B: NON-HERMITIAN SKIN MODE UNDER PMC BOUNDARY CONDITION

We consider a system sandwiched by two PMCs placed at $x = 0$ and $x = L$. The two PMCs require $H_z(0) = H_z(L) = 0$, which gives

$$\begin{pmatrix}1 & 1\\ e^{-ik_-L} & e^{-ik_+L}\end{pmatrix}\begin{pmatrix}A\\ B\end{pmatrix} = 0. \tag{B1}$$

The nontrivial solution of Eq. (B1) is derived when $k_+ - k_- = 2\pi n/L$. Therefore, $k_\pm$ and eigenfrequency under the PMC boundary condition are the same as those under the PEC boundary condition. The eigenmode is given by

$$H_z(x) = e^{iqk_yx}\sin\left(\frac{\pi n}{L}x\right), \tag{B2}$$

$$\begin{aligned}E_x(x) = -\frac{1}{2}ie^{iqk_yx}\Big[&(Z_{y+} - Z_{y-})\cos\left(\frac{\pi n}{L}x\right)\\ &- i(Z_{y+} + Z_{y-})\sin\left(\frac{\pi n}{L}x\right)\Big],\end{aligned} \tag{B3}$$

$$\begin{aligned}E_y(x) = \frac{1}{2}ie^{iqk_yx}\Big[&(Z_{x+} - Z_{x-})\cos\left(\frac{\pi n}{L}x\right)\\ &- i(Z_{x+} + Z_{x-})\sin\left(\frac{\pi n}{L}x\right)\Big].\end{aligned} \tag{B4}$$

The envelope of the eigenmode (B2)–(B4) exhibits exponential decay in the x direction when $\mathrm{Im}(qk_y) \neq 0$.

APPENDIX C: CALCULATION OF WINDING NUMBER

Here, we define the topological winding number of $\omega_{\rm PBC}^2$. To characterize the topological nature of a system, we use $\omega_{\rm PBC}^2$ instead of $\omega_{\rm PBC}$ because $\omega_{\rm PBC}^2$ is the eigenvalue of $\hat{\Theta}(k_y)$. Because the winding number does not change under the coordinate rotation and the shift of the origin, we consider the complex function $\lambda(t) = \lambda_1 + i\lambda_2$ defined by Eq. (A10) without loss generality. The winding number is defined by [48]

$$W(\lambda_0) = \frac{1}{2\pi}\int_{-\infty}^{\infty} dt \frac{d}{dt}\arg[\lambda(t) - \lambda_0], \tag{C1}$$

where λ_0 is a reference point on the complex plane.

The winding number can be analytically calculated. Here, we define $\Lambda(t) = [\lambda_2(t) - {\rm Im}(\lambda_0)]/[\lambda_1(t) - {\rm Re}(\lambda_0)]$ for simplicity. $\Lambda(t)$ converges to zero in the limit of $t \to \pm\infty$. We first consider a case when ${\rm Re}(\lambda_0) < -|\eta_{yy}|\{{\rm Im}(qk_y)\}^2$ [see the left panel of Fig. 7(c)]. In this case, $\lambda_1(t) - {\rm Re}(\lambda_0)$ satisfies $\lambda_1(t) - {\rm Re}(\lambda_0) > 0$ for all t. Therefore, the winding number is easily calculated as

$$W(\lambda_0) = \frac{1}{2\pi}[\tan^{-1}\Lambda(t)]_{t=-\infty}^{t=+\infty} = 0. \tag{C2}$$

Next, let us consider a case when λ_0 satisfies ${\rm Re}(\lambda_0) > -|\eta_{yy}|\{{\rm Im}(qk_y)\}^2$ and ${\rm Im}(\lambda_0) > 2|\eta_{yy}||{\rm Im}(qk_y)|t_1$ with

$$t_1 = \sqrt{\{{\rm Im}(qk_y)\}^2 + \frac{1}{|\eta_{yy}|}{\rm Re}(\lambda_0)}, \tag{C3}$$

as illustrated in the middle panel of Fig. 7(c). In this case, the winding number is calculated as

$$\begin{aligned} W(\lambda_0) &= \frac{1}{2\pi}[\tan^{-1}\Lambda(t)]_{t=-\infty}^{t=-t_1} + \frac{1}{2\pi}[\tan^{-1}\Lambda(t) - \pi]_{t=-t_1}^{t=t_1} \\ &\quad + \frac{1}{2\pi}[\tan^{-1}\Lambda(t)]_{t=t_1}^{t=+\infty} = 0. \end{aligned} \tag{C4}$$

Similarly, the winding number when λ_0 satisfies ${\rm Re}(\lambda_0) > -|\eta_{yy}|\{{\rm Im}(qk_y)\}^2$ and ${\rm Im}(\lambda_0) < -2|\eta_{yy}||{\rm Im}(qk_y)|t_1$ is calculated as

$$\begin{aligned} W(\lambda_0) &= \frac{1}{2\pi}[\tan^{-1}\Lambda(t)]_{t=-\infty}^{t=-t_1} + \frac{1}{2\pi}[\tan^{-1}\Lambda(t) + \pi]_{t=-t_1}^{t=t_1} \\ &\quad + \frac{1}{2\pi}[\tan^{-1}\Lambda(t)]_{t=t_1}^{t=+\infty} = 0. \end{aligned} \tag{C5}$$

Finally, we consider a case when λ_0 satisfies ${\rm Re}(\lambda_0) > -|\eta_{yy}|\{{\rm Im}(qk_y)\}^2$ and $|{\rm Im}(\lambda_0)| < 2|\eta_{yy}||{\rm Im}(qk_y)|t_1$. In this case, λ_0 is located inside a parabola, as illustrated in the right panel of Fig 7(c). Here, we define t_2 as

$$t_2 = \frac{{\rm Im}(\lambda_0)}{2|\eta_{yy}|{\rm Im}(qk_y)}, \tag{C6}$$

where t_2 satisfies $\lambda_2(t_2) = {\rm Im}(\lambda_0)$ and $-t_1 < t_2 < t_1$. The winding number is calculated as

$$\begin{aligned} W(\lambda_0) &= \frac{1}{2\pi}[\tan^{-1}\Lambda(t)]_{t=-\infty}^{t=-t_1} \\ &\quad + \frac{1}{2\pi}[\tan^{-1}\Lambda(t) - {\rm sgn}\{{\rm Im}(qk_y)\}\pi]_{t=-t_1}^{t=t_2} \\ &\quad + \frac{1}{2\pi}[\tan^{-1}\Lambda(t) + {\rm sgn}\{{\rm Im}(qk_y)\}\pi]_{t=t_2}^{t=t_1} \\ &\quad + \frac{1}{2\pi}[\tan^{-1}\Lambda(t)]_{t=t_1}^{t=+\infty} \\ &= -\,{\rm sgn}[{\rm Im}(qk_y)]. \end{aligned} \tag{C7}$$

In summary, the winding number $W(\lambda_0)$ is quantized to integers, and the winding number becomes ±1 if a reference point λ_0 is inside a parabola.

APPENDIX D: MIRROR-TIME SYMMETRY

The eigenfrequency $\omega_{\rm PEC}$, given by Eq. (16), is generally complex. The imaginary part of ω determines whether the eigenmode is attenuated $[{\rm Im}(\omega) > 0]$ or amplified $[{\rm Im}(\omega) < 0]$ in time. When ${\rm Im}(\eta_{yy}) > 0$ and ${\rm Im}(\eta_{xx} - q^2\eta_{yy}) > 0$, $\omega_{\rm PEC}$ satisfies ${\rm Im}(\omega_{\rm PEC}) > 0$ for all n and k_y (when k_y is assumed to be real). Similarly, $\omega_{\rm PEC}$ satisfies ${\rm Im}(\omega_{\rm PEC}) < 0$ for all n and k_y when ${\rm Im}(\eta_{yy}) < 0$ and ${\rm Im}(\eta_{xx} - q^2\eta_{yy}) < 0$. When ${\rm Im}(\eta_{yy}) = 0$ and ${\rm Im}(\eta_{xx} - q^2\eta_{yy}) = 0$, the reality of $\omega_{\rm PEC}^2$ is guaranteed for all n and k_y. A mirror-time symmetry sufficiently guarantees the reality of $\omega_{\rm PEC}^2$. The mirror-time symmetry holds when the diagonal components are real and off-diagonal components are pure imaginary as discussed below.

A mirror-time operation is the combination of a mirror operation and the time-reversal symmetry. We first consider a mirror operation with respect to the xz plane denoted by M_y. Because the M_y operation transforms (E_x, E_y) into $(-E_x, E_y)$, the M_x operation transforms ε as

$$\varepsilon' = \begin{pmatrix} \varepsilon_{xx} & -\varepsilon_{xy} \\ -\varepsilon_{yx} & \varepsilon_{yy} \end{pmatrix}. \tag{D1}$$

The time-reversal operation is represented by complex conjugation and transforms ε as $\varepsilon' = \varepsilon^*$. The mirror-time (M_yT) operation transforms ε as

$$\varepsilon' = \begin{pmatrix} \varepsilon_{xx}^* & -\varepsilon_{xy}^* \\ -\varepsilon_{yx}^* & \varepsilon_{yy}^* \end{pmatrix}. \tag{D2}$$

The M_yT symmetry for ε is represented by $\varepsilon' = \varepsilon$. Therefore, a system is invariant under the M_yT symmetry when the diagonal components are real and off-diagonal components are pure imaginary. The M_yT operation transforms $\hat{\Theta}(k_y)$ as $\hat{\Theta}'(k_y) = (M_yT)^{-1}\hat{\Theta}(k_y)(M_yT)$, where $\hat{\Theta}'(k_y)$ can be derived by complex conjugation as

$$\hat{\Theta}'(k_y) = -\eta_{yy}^*\frac{d^2}{dx^2} + ik_y(\eta_{xy}^* + \eta_{yx}^*)\frac{d}{dx} + \eta_{xx}^*k_y^2. \tag{D3}$$

When $\varepsilon' = \varepsilon$, $\hat{\Theta}(k_y)$ satisfies the M_yT symmetry represented by $\hat{\Theta}(k_y) = (M_yT)^{-1}\hat{\Theta}(k_y)(M_yT)$. The M_yT symmetry leads to $(\omega^2)^* = \omega^2$. If an eigenmode is nondegenerate, the reality of ω^2 is guaranteed by the M_yT symmetry although $\hat{\Theta}(k_y)$ is non-Hermitian. In M_yT-symmetric systems, skin modes have real eigenfrequencies.

APPENDIX E: TIME-AVERAGED POYNTING VECTOR

The time-averaged Poynting vector is well defined only when ω is real. In this section, we discuss the time-averaged

Poynting vector and power flow of a stationarily excited skin mode. The mode profile of a stationarily excited mode can be recast as

$$H_z(x) = -\frac{i}{2}e^{iqk_yx}\left[\frac{1}{Z_{x-}}e^{(i\pi n/L)x} - \frac{1}{Z_{x+}}e^{-(i\pi n/L)x}\right], \tag{E1}$$

$$E_x(x) = \frac{i}{2}e^{iqk_yx}\left[\frac{Z_{y-}}{Z_{x-}}e^{(i\pi n/L)x} - \frac{Z_{y+}}{Z_{x+}}e^{-(i\pi n/L)x}\right]. \tag{E2}$$

The y component of the time-averaged Poynting vector $S_y = (-1/2)\mathrm{Re}(E_xH_z^*)$ is calculated as

$$S_y(x,y) = \frac{1}{8}e^{-2\mathrm{Im}(qk_y)x+2\mathrm{Im}(k_y)y}\mathrm{Re}\left[\frac{Z_{y-}}{|Z_{x-}|^2} + \frac{Z_{y+}}{|Z_{x+}|^2} - \frac{Z_{y-}}{Z_{x+}^*Z_{x-}}e^{i(2\pi n/L)x} - \frac{Z_{y+}}{Z_{x+}Z_{x-}^*}e^{-i(2\pi n/L)x}\right]. \tag{E3}$$

The power flow through the waveguide is defined by the integral of S_y,

$$P_y(y) = e^{2\mathrm{Im}(k_y)y}\int_0^L dxS_y(x,y). \tag{E4}$$

The power flow determines the propagation direction. If $\mathrm{Im}(k_y)P_y < 0$, the waveguide mode is lossy.

APPENDIX F: LEFT EIGENMODE OF EQ. (2)

The transpose of a differential operator is defined by integration by parts [70]. The transpose of $\hat{\Theta}(k_y)$ is given by [11]

$$\begin{aligned}\hat{\Theta}^T(k_y) &= -\eta_{yy}\frac{d^2}{dx^2} + 2ik_y(\eta_{xy}+\eta_{yx})\frac{d}{dx} + k_y^2\eta_{xx}\\ &= \hat{\Theta}(-k_y).\end{aligned} \tag{F1}$$

Equation (F1) shows that the left eigenmode of $\hat{\Theta}(k_y)$ is just the right eigenmode of $\hat{\Theta}(-k_y)$. The left eigenmode of $\hat{\Theta}(k_y)$ under the PEC boundary condition is given by

$$E^L_{y,k_y,n}(x) = e^{-iqk_yx}\sin\left(\frac{\pi n}{L}x\right), \tag{F2}$$

$$\begin{aligned}H^L_{z,k_y,n}(x) = \frac{1}{2}ie^{-iqk_yx}\Bigg[&\left(\frac{1}{Z_{x+}} - \frac{1}{Z_{x-}}\right)\cos\left(\frac{\pi n}{L}x\right)\\ &- i\left(\frac{1}{Z_{x+}} + \frac{1}{Z_{x-}}\right)\sin\left(\frac{\pi n}{L}x\right)\Bigg],\end{aligned} \tag{F3}$$

$$\begin{aligned}E^L_{x,k_y,n}(x) = -\frac{1}{2}ie^{-iqk_yx}\Bigg[&\left(\frac{Z_{y+}}{Z_{x+}} - \frac{Z_{y-}}{Z_{x-}}\right)\cos\left(\frac{\pi n}{L}x\right)\\ &- i\left(\frac{Z_{y+}}{Z_{x+}} + \frac{Z_{y+}}{Z_{x-}}\right)\sin\left(\frac{\pi n}{L}x\right)\Bigg].\end{aligned} \tag{F4}$$

The left eigenmode is localized at the opposite side to the right eigenmode. We can easily prove the orthogonal relation by using the orthogonality of sine and cosine:

$$\int_0^L H^L_{z,mk_y}(x)H^R_{z,nk_y}(x)dx \propto \delta_{mn}. \tag{F5}$$

---

[1] L. Feng, R. El-Ganainy, and L. Ge, Non-Hermitian photonics based on parity–time symmetry, Nat. Photon. **11**, 752 (2017).

[2] R. El-Ganainy, K. G. Makris, M. Khajavikhan, Z. H. Musslimani, S. Rotter, and D. N. Christodoulides, Non-Hermitian physics and PT symmetry, Nat. Phys. **14**, 11 (2018).

[3] Ş. K. Özdemir, S. Rotter, F. Nori, and L. Yang, Parity–time symmetry and exceptional points in photonics, Nat. Mater. **18**, 783 (2019).

[4] Y. Ota, K. Takata, T. Ozawa, A. Amo, Z. Jia, B. Kante, M. Notomi, Y. Arakawa, and S. Iwamoto, Active topological photonics, Nanophotonics **9**, 547 (2020).

[5] S. Yao and Z. Wang, Edge states and topological invariants of non-Hermitian systems, Phys. Rev. Lett. **121**, 086803 (2018).

[6] S. Yao, F. Song, and Z. Wang, Non-Hermitian Chern bands, Phys. Rev. Lett. **121**, 136802 (2018).

[7] K. Yokomizo and S. Murakami, Non-Bloch band theory of non-Hermitian systems, Phys. Rev. Lett. **123**, 066404 (2019).

[8] D. S. Borgnia, A. J. Kruchkov, and R.-J. Slager, Non-Hermitian boundary modes and topology, Phys. Rev. Lett. **124**, 056802 (2020).

[9] N. Okuma, K. Kawabata, K. Shiozaki, and M. Sato, Topological origin of non-Hermitian skin effects, Phys. Rev. Lett. **124**, 086801 (2020).

[10] K. Kawabata, N. Okuma, and M. Sato, Non-Bloch band theory of non-Hermitian Hamiltonians in the symplectic class, Phys. Rev. B **101**, 195147 (2020).

[11] J. Zhong, K. Wang, Y. Park, V. Asadchy, C. C. Wojcik, A. Dutt, and S. Fan, Nontrivial point-gap topology and non-Hermitian skin effect in photonic crystals, Phys. Rev. B **104**, 125416 (2021).

[12] Q. Yan, H. Chen, and Y. Yang, Non-Hermitian skin effect and delocalized edge states in photonic crystals with anomalous parity-time symmetry, Prog. Electromagn. Res. **172**, 33 (2021).

[13] K. Yokomizo, T. Yoda, and S. Murakami, Non-Hermitian waves in a continuous periodic model and application to photonic crystals, Phys. Rev. Res. **4**, 023089 (2022).

[14] Z. Fang, M. Hu, L. Zhou, and K. Ding, Geometry-dependent skin effects in reciprocal photonic crystals, Nanophotonics **11**, 3447 (2022).

[15] T. Ochiai, Non-Hermitian skin effect and lasing of absorbing open-boundary modes in photonic crystals, Phys. Rev. B **106**, 195412 (2022).

[16] W. Zhu and J. Gong, Photonic corner skin modes in non-Hermitian photonic crystals, Phys. Rev. B **108**, 035406 (2023).

[17] A. Poddubny, J. Zhong, and S. Fan, Mesoscopic non-Hermitian skin effect, Phys. Rev. A **109**, L061501 (2024).

[18] M. Brandenbourger, X. Locsin, E. Lerner, and C. Coulais, Non-reciprocal robotic metamaterials, Nat. Commun. **10**, 4608 (2019).

[19] A. Ghatak, M. Brandenbourger, J. Van Wezel, and C. Coulais, Observation of non-Hermitian topology and its bulk–edge correspondence in an active mechanical metamaterial, Proc. Natl. Acad. Sci. USA **117**, 29561 (2020).

[20] Y. Chen, X. Li, C. Scheibner, V. Vitelli, and G. Huang, Realization of active metamaterials with odd micropolar elasticity, Nat. Commun. **12**, 5935 (2021).

[21] T. Helbig, T. Hofmann, S. Imhof, M. Abdelghany, T. Kiessling, L. Molenkamp, C. Lee, A. Szameit, M. Greiter, and R. Thomale, Generalized bulk–boundary correspondence in non-Hermitian topolectrical circuits, Nat. Phys. **16**, 747 (2020).

[22] S. Liu, R. Shao, S. Ma, L. Zhang, O. You, H. Wu, Y. J. Xiang, T. J. Cui, and S. Zhang, Non-Hermitian skin effect in a non-Hermitian electrical circuit, Research **2021**, 5608038 (2021).

[23] T. Hofmann, T. Helbig, F. Schindler, N. Salgo, M. Brzezińska, M. Greiter, T. Kiessling, D. Wolf, A. Vollhardt, A. Kabaši, C. H. Lee, A. Bilušić, R. Thomale, and T. Neupert, Reciprocal skin effect and its realization in a topolectrical circuit, Phys. Rev. Res. **2**, 023265 (2020).

[24] D. Zou, T. Chen, W. He, J. Bao, C. H. Lee, H. Sun, and X. Zhang, Observation of hybrid higher-order skin-topological effect in non-Hermitian topolectrical circuits, Nat. Commun. **12**, 7201 (2021).

[25] S. Weidemann, M. Kremer, T. Helbig, T. Hofmann, A. Stegmaier, M. Greiter, R. Thomale, and A. Szameit, Topological funneling of light, Science **368**, 311 (2020).

[26] L. Xiao, T. Deng, K. Wang, G. Zhu, Z. Wang, W. Yi, and P. Xue, Non-Hermitian bulk–boundary correspondence in quantum dynamics, Nat. Phys. **16**, 761 (2020).

[27] X. Zhang, Y. Tian, J.-H. Jiang, M.-H. Lu, and Y.-F. Chen, Observation of higher-order non-Hermitian skin effect, Nat. Commun. **12**, 5377 (2021).

[28] L. Zhang, Y. Yang, Y. Ge, Y.-J. Guan, Q. Chen, Q. Yan, F. Chen, R. Xi, Y. Li, D. Jia, S.-Q. Yuan, H.-X. Sun, H. Chen, and B. Zhang, Acoustic non-Hermitian skin effect from twisted winding topology, Nat. Commun. **12**, 6297 (2021).

[29] Z. Gu, H. Gao, H. Xue, J. Li, Z. Su, and J. Zhu, Transient non-Hermitian skin effect, Nat. Commun. **13**, 7668 (2022).

[30] Q. Zhou, J. Wu, Z. Pu, J. Lu, X. Huang, W. Deng, M. Ke, and Z. Liu, Observation of geometry-dependent skin effect in non-Hermitian phononic crystals with exceptional points, Nat. Commun. **14**, 4569 (2023).

[31] Y. G. Liu, Y. Wei, O. Hemmatyar, G. G. Pyrialakos, P. S. Jung, D. N. Christodoulides, and M. Khajavikhan, Complex skin modes in non-Hermitian coupled laser arrays, Light Sci. Appl. **11**, 336 (2022).

[32] T. Liu, Y.-R. Zhang, Q. Ai, Z. Gong, K. Kawabata, M. Ueda, and F. Nori, Second-order topological phases in non-Hermitian systems, Phys. Rev. Lett. **122**, 076801 (2019).

[33] K. Kawabata, M. Sato, and K. Shiozaki, Higher-order non-Hermitian skin effect, Phys. Rev. B **102**, 205118 (2020).

[34] T. Yoshida, T. Mizoguchi, and Y. Hatsugai, Mirror skin effect and its electric circuit simulation, Phys. Rev. Res. **2**, 022062(R) (2020).

[35] C. Scheibner, W. T. M. Irvine, and V. Vitelli, Non-Hermitian band topology and skin modes in active elastic media, Phys. Rev. Lett. **125**, 118001 (2020).

[36] R. Okugawa, R. Takahashi, and K. Yokomizo, Second-order topological non-Hermitian skin effects, Phys. Rev. B **102**, 241202(R) (2020).

[37] R. Okugawa, R. Takahashi, and K. Yokomizo, Non-Hermitian band topology with generalized inversion symmetry, Phys. Rev. B **103**, 205205 (2021).

[38] K. Zhang, Z. Yang, and C. Fang, Universal non-Hermitian skin effect in two and higher dimensions, Nat. Commun. **13**, 2496 (2022).

[39] K. Yokomizo and S. Murakami, Non-Bloch bands in two-dimensional non-Hermitian systems, Phys. Rev. B **107**, 195112 (2023).

[40] L. D. Landau, J. Bell, M. Kearsley, L. Pitaevskii, E. Lifshitz, and J. Sykes, *Electrodynamics of Continuous Media* (Elsevier, Amsterdam, 2013), Vol. 8.

[41] F. Liu and J. Li, Gauge field optics with anisotropic media, Phys. Rev. Lett. **114**, 103902 (2015).

[42] Y. Chen, R.-Y. Zhang, Z. Xiong, Z. H. Hang, J. Li, J. Q. Shen, and C. T. Chan, Non-Abelian gauge field optics, Nat. Commun. **10**, 3125 (2019).

[43] N. Hatano and D. R. Nelson, Localization transitions in non-Hermitian quantum mechanics, Phys. Rev. Lett. **77**, 570 (1996).

[44] S. M. Hashemi and I. S. Nefedov, Wideband perfect absorption in arrays of tilted carbon nanotubes, Phys. Rev. B **86**, 195411 (2012).

[45] I. S. Nefedov, C. A. Valagiannopoulos, S. M. Hashemi, and E. I. Nefedov, Total absorption in asymmetric hyperbolic media, Sci. Rep. **3**, 2662 (2013).

[46] I. S. Nefedov, C. A. Valagiannopoulos, and L. A. Melnikov, Perfect absorption in graphene multilayers, J. Opt. **15**, 114003 (2013).

[47] S. Debnath, E. Khan, and E. E. Narimanov, Incoherent perfect absorption in lossy anisotropic materials, Opt. Express **27**, 9561 (2019).

[48] S. Longhi, Non-Hermitian skin effect beyond the tight-binding models, Phys. Rev. B **104**, 125109 (2021).

[49] M. G. Silveirinha, Chern invariants for continuous media, Phys. Rev. B **92**, 125153 (2015).

[50] Z. Zhao, C. Guo, and S. Fan, Connection of temporal coupled-mode-theory formalisms for a resonant optical system and its time-reversal conjugate, Phys. Rev. A **99**, 033839 (2019).

[51] S. Buddhiraju, A. Song, G. T. Papadakis, and S. Fan, Nonreciprocal metamaterial obeying time-reversal symmetry, Phys. Rev. Lett. **124**, 257403 (2020).

[52] C. Guo, Z. Zhao, and S. Fan, Internal transformations and internal symmetries in linear photonic systems, Phys. Rev. A **105**, 023509 (2022).

[53] A. Yariv and P. Yeh, *Photonics: Optical Electronics in Modern Communications* (Oxford University Press, Oxford, 2007).

[54] P. B. Johnson and R. W. Christy, Optical constants of the noble metals, Phys. Rev. B **6**, 4370 (1972).

[55] A. Poddubny, I. Iorsh, P. Belov, and Y. Kivshar, Hyperbolic metamaterials, Nat. Photon. **7**, 948 (2013).

[56] E. E. Narimanov and A. V. Kildishev, Naturally hyperbolic, Nat. Photon. **9**, 214 (2015).

[57] J. D. Jackson, *Classical Electrodynamics* (John Wiley & Sons, Hoboken, 1999).

[58] D. M. Pozar, *Microwave Engineering* (John Wiley & Sons, Hoboken, 2011).

[59] M. Davanço, Y. Urzhumov, and G. Shvets, The complex Bloch bands of a 2D plasmonic crystal displaying isotropic negative refraction, Opt. Express **15**, 9681 (2007).

[60] C. Fietz, Y. Urzhumov, and G. Shvets, Complex k band diagrams of 3D metamaterial/photonic crystals, Opt. Express **19**, 19027 (2011).

[61] G. Parisi, P. Zilio, and F. Romanato, Complex Bloch-modes calculation of plasmonic crystal slabs by means of finite elements method, Opt. Express **20**, 16690 (2012).

[62] X. Gao, B. Zhen, M. Soljačić, H. Chen, and C. W. Hsu, Bound states in the continuum in fiber Bragg gratings, ACS Photon. **6**, 2996 (2019).

[63] H. Schomerus, Nonreciprocal response theory of non-Hermitian mechanical metamaterials: Response phase transition from the skin effect of zero modes, Phys. Rev. Res. **2**, 013058 (2020).

[64] H. Schomerus, Fundamental constraints on the observability of non-Hermitian effects in passive systems, Phys. Rev. A **106**, 063509 (2022).

[65] F. D. M. Haldane and S. Raghu, Possible realization of directional optical waveguides in photonic crystals with broken time-reversal symmetry, Phys. Rev. Lett. **100**, 013904 (2008).

[66] S. Raghu and F. D. M. Haldane, Analogs of quantum-Hall-effect edge states in photonic crystals, Phys. Rev. A **78**, 033834 (2008).

[67] Z. Wang, Y. D. Chong, J. D. Joannopoulos, and M. Soljačić, Reflection-free one-way edge modes in a gyromagnetic photonic crystal, Phys. Rev. Lett. **100**, 013905 (2008).

[68] Z. Wang, Y. Chong, J. D. Joannopoulos, and M. Soljačić, Observation of unidirectional backscattering-immune topological electromagnetic states, Nature (London) **461**, 772 (2009).

[69] C. Scheibner, A. Souslov, D. Banerjee, P. Surówka, W. T. Irvine, and V. Vitelli, Odd elasticity, Nat. Phys. **16**, 475 (2020).

[70] A. E. Siegman, *Lasers* (University Science Books, Melville, 1986).